A FEASIBILITY ASSESSMENT OF USING ULTRASONIC SENSOR POSITION FEEDBACK FOR A BALL-AND-BEAM APPARATUS

by

JACOB DANIEL WIENEKE

B.S., Kansas State University, 2008

A THESIS

submitted in partial fulfillment of the requirements for the degree

MASTER OF SCIENCE

Department of Mechanical and Nuclear Engineering
College of Engineering

KANSAS STATE UNIVERSITY
Manhattan, Kansas

2010

Approved by:

Major Professor
Warren N. White

Copyright

Abstract

This thesis describes the process of testing and implementing ultrasonic transducers for ball position feedback on a ball-and-beam apparatus. Also included are specifications for equipment to allow feedback and command signals to be wireless, not hardwired to the control computer. The author presents various ball-and-beam configurations as well as details about the specific configuration used for this work. These details include choices in sensors, materials, hardware, construction, and controller. After the apparatus has been described, the author provides information to support claims about system performance. The conclusions presented specify the necessary hardware to make the system wireless and indicate that acoustic sensors can complete a successful ball-on-beam balancing system.

Table of Contents

List of Figures

List of Tables

Acknowledgements

The author wishes to acknowledge students J. Chavira, E. Martinez, N. Rauth, and V. Salazar who contributed to the development and construction of the hardware set-up and assisted with the model creation and parameter identification.

For their service on the committee, the author wishes to acknowledge Dr. Schinstock and Dr. Hu.

The author also gratefully acknowledges the assistance of Dr. White throughout the process of completing this work.

Dedication

This work is dedicated to my wife, Amy, and to my parents, siblings, and friends whose love and support made it possible.

CHAPTER 1 - Introduction

The ball-and-beam setup has been used regularly in controls education to study the problem of underactuated mechanical systems. The purpose of this thesis is to explore the use of ultrasonic sensors to determine the position of the ball and specify possible equipment to give the system wireless capabilities. This chapter will present different options for developing a ball-and-beam apparatus, including the physical construction and the sensor selection.

Ball-and-Beam Variations

The basic construction of the apparatus can vary, but the principles remain the same: a ball rolls freely on a beam and the angle of the beam can be changed. There are sensors present to determine the location of the ball on the beam and the angle of the beam. A controller is developed to either stabilize the ball at some desired location on the beam or to have the ball track a reference trajectory.

Beam Configurations

The ball-and-beam can be constructed several different ways as discussed below. Regardless of the implementation, the system produces a change in beam angle based on a corresponding change in motor angular position.

Fixed-End Beam Construction

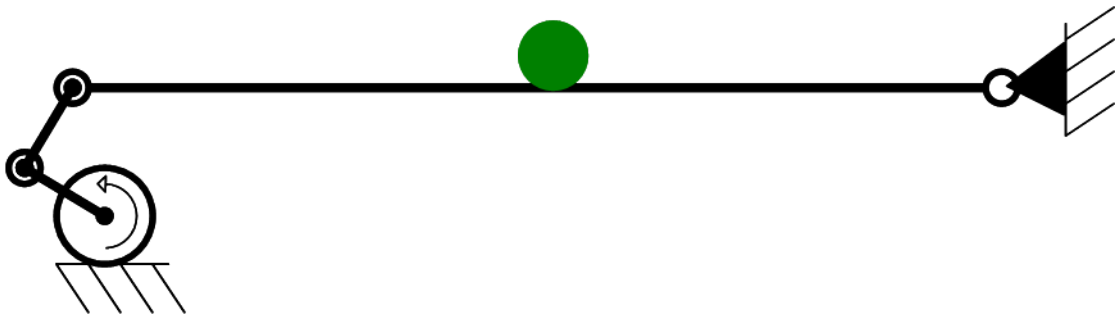

Figure 1-1 Fixed-End Beam

In the configuration shown in Figure 1-1, one end of the beam is fixed to a rotational joint and the other is connected to a motor by a linkage, allowing the pitch of the beam to be controlled. There is a commercial version of this construction available from Quanser (Quanser Inc.).

Rotational Beam Interface

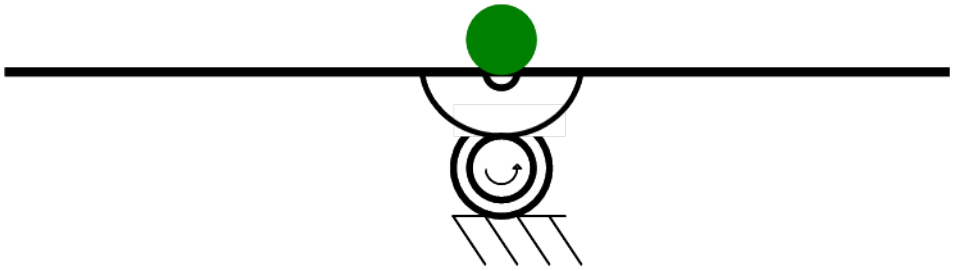

Figure 1-2 Rotational Beam Interface

As shown in Figure 1-2, this implementation allows the motor to manipulate the beam angle by rotating a disk on the motor shaft that counter-rotates a semicircular disk affixed to the beam. The beam rotates about a fixed point at its center. This method of construction was used at MIT for creating a set-up to be used in an undergraduate class (Rosales). Instead of a disk, it would be possible to use a gear system, which would reduce the slipping problems discovered by Ito (Ito).

Motor-Mounted Beam Construction

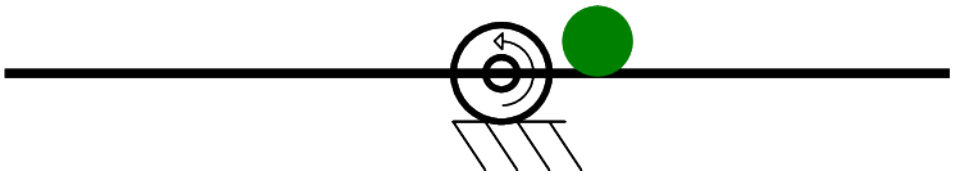

Figure 1-3 Motor-Mounted Beam

The implementation shown in Figure 1-3, with an offset, was selected for this work. The beam center is attached to the motor shaft directly (Ito; Situm 225-234). This eliminates problems caused by slipping in the drive train, such as undetermined positions, as experienced by Ito, which were then solved by opting for a direct-mount construction (Ito).

Sensor Selection

There are many options available to monitor the angle of the beam and the position of the ball. A few of the more common choices are reviewed here, but this list is not intended to be exhaustive.

Beam Angle Sensor

The beam angle can be determined using a potentiometer attached to the beam shaft (Rosales) or attached to the rear of the actuator shaft (Situm 225-234). A second option is an

accelerometer which can be utilized with its measured acceleration proportional to the sine of the beam angle (Ito). Another method, the one used for this thesis, is to have an angular encoder on the rear shaft of the motor (Rosales), allowing the determination of the beam angle directly, when the beam is mounted directly to the motor shaft or connected by a transmission system.

Ball Position Sensor

Arguably the most difficult task in the construction of a ball-and-beam apparatus is selecting a sensor to determine the position of the ball. Finding or constructing a sensor with high resolution and low noise that can determine the ball position reliably and accurately can require significant cost.

Rosales tested several versions of linear potentiometers based on the ball being conductive and passing current from one rail to another (Rosales). In this method, one rail is electrified with a constant current producing a linear distribution of voltage along the rail; the voltage of the other rail is monitored to determine the ball position. As the ball rolls on the rails it causes a change in voltage that can be measured and used in conjunction with the known rail resistance to determine where on the length of wire, and thus the beam, the ball is located. This method was used in prior and current ball-and-beam projects (Rosales; Ito; Situm 225-234; Rosales et al. 1314-1318 vol.2; Sheng, Renner and Levine 402-408). The major benefit to this type of sensor is that it is available for very little cost (Rosales et al. 1314-1318 vol.2). A downfall to this method is the noise generated by the ball rolling on the track and the possible loss of signal due to pits and irregularities, depending on the track type selected (Rosales; Ito). Depending on the rail configuration, sliding friction could be introduced at the point of contact with the ball, a disadvantage illustrated in the second option shown in Figure 1-4.

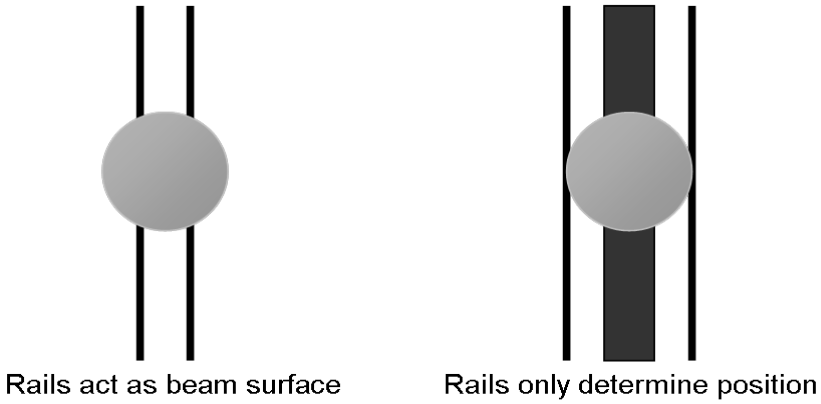

Figure 1-4 Conductive rail configurations

Infrared range (IR) finders could be used as an alternative as mentioned in (Rosales et al. 1314-1318 vol.2). This possibility was explored when an IR sensor was tested by Ito (Ito). Because these sensors have an inherently nonlinear response, Ito concluded that systems incorporating this type of sensor would require the ability to operate using a range of gains and varying ball position uncertainty (Ito). A benefit to using this type of sensor is that it provides non-contact monitoring of the ball position. Drawbacks of these sensors are their limited operating range and lack of precision when detecting a spherical object.

Laser range finders are another non-contact method of measuring a position. However, the available commercial versions are either too expensive or have a range that is too limited to measure a ball's position on desired beam lengths.

A final sensor alternative is ultrasonic transducers (Rosales et al. 1314-1318 vol.2). Situm explored this as an option and discarded it in favor of the linear potentiometer method, because the particular sensor tested had a relatively short range of measurement (Situm 225-234). Like IR sensors, the benefit to ultrasonic sensors is non-contact measuring of the ball position. Disadvantages to using ultrasonic sensors include limited ranges (depending on sensor and configuration) and cost of the sensor. Despite these disadvantages, an ultrasonic sensor was selected as the method to measure the ball position for this work, because it was a non-contact alternative that could measure the ball position over the length of the beam.

CHAPTER 2 - Specific Construction

The ball-and-beam construction chosen for this thesis is described in this chapter. The sensors chosen for measurements together with the materials and design of the beam are described as well as the choice of motor, amplifier, ball, control hardware, and possible wireless hardware.

This ball-and-beam is a stepping stone toward building an inverted pendulum cart that will balance a ball on a beam that is fixed to the top of the pendulum, as illustrated in Figure 2-1.

Figure 2-1 Ball-and-Beam Inverted Pendulum Cart

It is desired to control that cart wirelessly, with the controller not onboard, which is the motivation for determining the appropriate wireless hardware. The ball-and-beam assembly was completed after a few design iterations in order to complement hardware choices that had been made for the aforementioned cart.

Ball Sensor

An ultrasonic sensor was selected for this project to avoid any introduction of sliding friction for the ball and to allow accurate measurement of the position of a ball that could be made of non-conductive material, which provides a greater selection in ball candidates. The linear potentiometer sensor variants require that a conductive ball be used; otherwise a current cannot be passed from the electrified rail to the measurement rail. Depending on the

configuration of these rails the ball could be required to slide along the rails, instead of roll, which introduces sliding friction into the system dynamics. To overcome these shortfalls the decision was made to pick a non-contact position sensor. After researching possible infrared and laser optical sensors it was determined that the measuring range of commercially available sensors was not well suited to the proposed beam length. The choice was made to investigate ultrasonic sensors as a means of obtaining non-contact position measurement. The Senix ToughSonic series appeared to be capable of detecting various ball sizes over the required distance, with a limitation that objects closer than about four inches cannot be correctly detected by the sensor. The final sensor selected was a TSPC-30S1-232 from Senix. It can be configured using a PC and the provided SenixVIEW software so that the analog 0-10 Volt output is scaled to represent the desired range. The sensor requires 10-30 Volts DC to be powered, but its sensitivity is reduced below 15 Volts (Senix Corporation).

One consideration for acoustic sensors placed at opposing ends of the beam is that they may receive ultrasonic waves from each other, causing inaccurate measurements. Another is their ability to accurately determine the ball's position over the specified range of the beam. These will be discussed further in a later chapter.

Beam Construction

The beam had to meet several requirements based on its inclusion with the future project. It needed to be lightweight, allow the ball to roll without slip, and be able to support the ultrasonic sensors. Aluminum was chosen for the beam material to satisfy the weight requirement. Two different extrusion options were considered, angled and U-channel. The angled aluminum was selected because it required less material and offered a rolling surface that 'cradled' the ball instead of just supporting it.

Sensor brackets were then designed and machined from aluminum blocks and attached to the beam. These brackets allow the sensors to point along the beam axis directed at the center of the ball, while offering protection from the ball rolling directly against the sensor surface. The beam center is attached to a milled aluminum block that has a shaft press-fit into it that allows rotation about the beam's central axis. As noted later, this introduced changes in the form of additional moments to the assumed dynamics because of the offset between the surface that the ball rolls on and the beam rotation.

Motor and Amplifier

Both the motor and amplifier choice were determined by equipment availability. The motor that provides actuation to the beam rotational axis is a Reliance Electric brushless DC motor model BDC-T330-BVL. The motor has a Danaher Industrial Controls optical encoder model M20250011001 attached to the rear shaft for angular position measurement. Connected to this motor is an Advanced Motion Controls brushless PWM servo amplifier model CBE25ACB. This amplifier allows current control of the motor, supplying a current that is proportional to the amplifier input voltage. The amplifier has a rectifier built-in and can be plugged directly into 25-130 Volt AC outlets (Advanced Motion Controls).

The motor shaft is connected by a coupler to the shaft of the beam assembly, which allows the actuation of the beam. This connection method also directly couples the beam angle to the motor angle, allowing the beam angle to be determined by using the optical encoder attached to the motor.

Ball

Several ball options were considered during the construction of the system. Originally, a ping-pong ball was desired because of its low inertia and availability. However, the ping-pong ball with its small diameter initially made it difficult for the ultrasonic sensor to accurately determine its position. The next option was five inches in diameter and liquid-filled, but that was quickly phased out for something smaller and not liquid-filled in order to avoid the additional complications of the extra weight. A croquet ball and a toy foam ball were both tried, but neither was sufficiently smooth to facilitate easy rolling on the beam surface. Finally, a standard racquetball was chosen to complete the apparatus. The racquetball is an attractive choice due to the sensor being able to determine its location, its low inertia, its cost, and its availability.

Controller Hardware

The hardware for the controller of the system was selected based on two factors, compatibility and availability. Due to a recent lab renovation, real-time desktop PC's were readily available and running NI LabVIEW Real Time with NI PCIe-6361 X-series DAQs already purchased and installed. These two crucial pieces for a controller, communication and computation, were readily available and already designed to work together.

System Wiring

To complete the system, the sensors and amplifier inputs needed to be connected to the controller through the inputs and outputs of the PCIe-6361. This was facilitated by the use of the NI CB-68LPR, which provides screw-terminal access to the pins of the PCIe-6361. The wiring chart for the ball-and-beam system is provided in Table 2.1 and illustrated in Figure 2-2. It is important to note that the acoustic sensor grounds (blue of sensors 1 and 2) are connected to DAQ analog negative reference, analog in ground, and the voltage source ground. Also shown are the connections necessary for the final acoustic sensor configuration discussed in Chapter 5.

Table 2.1 System Wiring Chart

Sensor Wire	Function	Wire to	NI Board Terminal	NI PCIe-6361 Channel
Sensor 1 White	0-10 V	→	33	Analog In 1 +
Sensor 1 Blue	Ground	→	66 & 32	Analog In 1 - & AI GND
Sensor 2 White	0-10 V	→	65	Analog In 2 +
Sensor 2 Blue	Ground	→	31 & 64	Analog In 2 - & AI GND
Motor Encoder				
Red	Vcc	→	14	+ 5 V
Black	Ground	→	15	GND
Green	Channel A	→	42	Counter 1 A
Orange	Channel B	→	46	Counter 1 B
White	Z index	→	41	Counter 1 Z
Amp Pin P1				
4	+ REF IN	→	22	Analog Out 0
5	- REF IN	→	55	Analog Out GND
			Motor Wire	
10	+ VHALL 30mA OUT	→	Pink	
11	GROUND	→	Black	
12	HALL 1	→	Yellow	
13	HALL 2	→	White	
14	HALL 3	→	Orange	
Amp Pin P2				
1	Motor A	→	Blue	
2	Motor B	→	Brown	
3	Motor C	→	Purple	
Sensor Wire			**Sensor Wire**	
Sensor 1 Yellow	RS-485 +	→	Sensor 2 Yellow	
Sensor 1 Gray	RS-485 -	→	Sensor 2 Gray	
			Voltage Source	
Sensor 1 Brown	+ DC IN Voltage	→	+ VDC	
Sensor 1 Blue	- DC IN & Signal GND	→	-VDC	
Sensor 2 Brown	+ DC IN Voltage	→	+ VDC	
Sensor 2 Blue	- DC IN & Signal GND	→	-VDC	

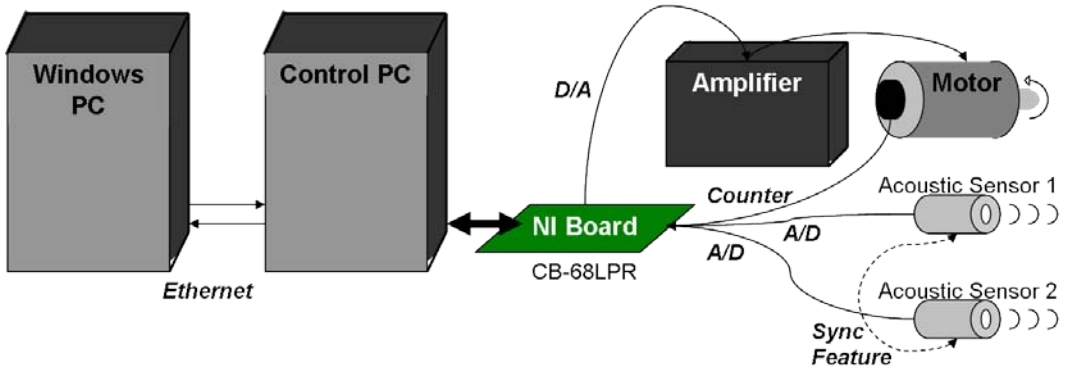

Figure 2-2 Current wiring configuration of system

Wireless Hardware

In order to separate the controller from the apparatus, some form of wireless instrumentation needs to be implemented. The author recommends the following configuration to get the system to fully realize this separation. National Instruments provides wireless data acquisition products that operate on the IEEE 802.11 wireless communication standard (Wi-Fi).

Specifically, the NI WLS-9472 provides eight digital output channels that could be combined with a digital-to-analog converter to allow the controller to pass commands wirelessly to the amplifier (National Instruments Corporation). To achieve a higher resolution for the control signal it is recommended that two units be purchased, as this product provides the most output channels available from the National Instruments Wi-Fi products.

In order to wirelessly obtain the measurements from the apparatus, the author recommends the NI WLS-9205 which provides 32 single-ended or 16 differential analog inputs (National Instruments Corporation). These inputs could be configured to receive the ultrasonic sensor voltages and either individual encoder channel pulses or a digital input that uses a channel for each bit, with a quadrature decoding counter circuit between the motor encoder and the input to convert the encoder signal to a digital signal. Figure 2-3 provides a high-level block diagram of the proposed setup.

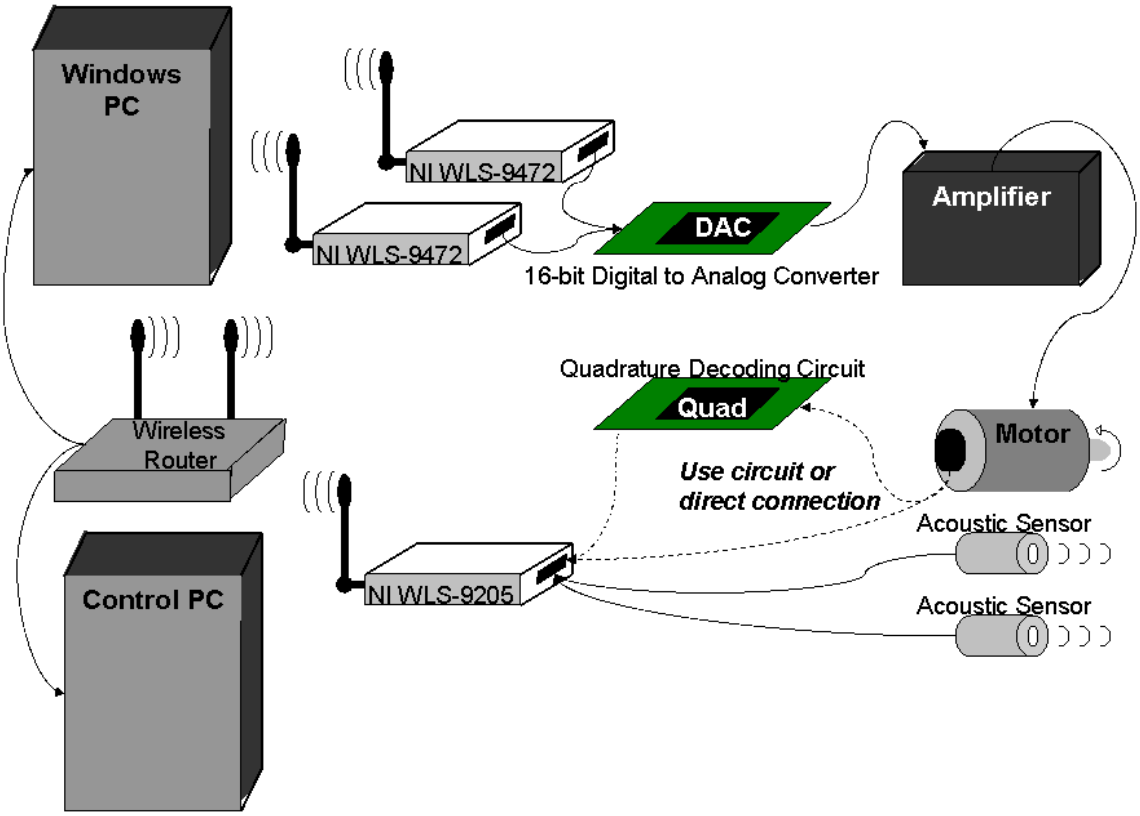

Figure 2-3 Illustration of proposed apparatus connections

CHAPTER 3 - System Model

In order to develop a controller for the ball-and-beam, a system model was developed that could be utilized when performing the pole-placement operation. Based on the system diagram a mathematical model of the system was formed, which assisted to specify which system parameters needed to be identified.

System Diagram

The system free body diagram, shown in Figure 3-1, was developed to accurately capture the forces and moments present in the designed ball-and-beam apparatus. One of the most notable features of the system used in this work is the offset distance between the point of rotation of the beam and the surface the ball rolls on; the similar systems researched had the two points coincident. This required careful consideration when determining the dynamic equations, to insure that the mathematical model of the system accurately captured how the system behaved. It is also important to note the difference introduced by the beam selection between R_o and R_{ball}; R_{ball} is the radius of the ball and R_o is the distance from the ball's center to the surface it is rolling on. The coordinate directions, distances, and forces are shown in Figure 3-1. For a listing of parameters and their values see Table 3.2.

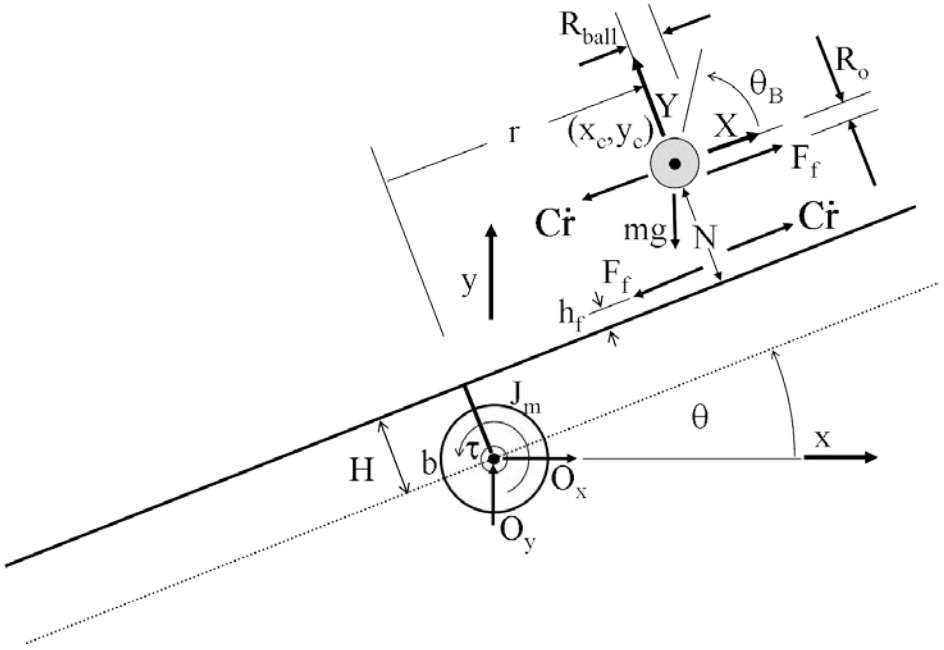

Figure 3-1 Ball-and-Beam Free Body Diagram

Dynamic Equations

The dynamic equations were determined by using the symbolic manipulator Maple. This operation was completed two ways, through classical mechanics and Lagrangian analysis. First, using classical mechanics, the center of the ball (x_c, y_c) was written in terms of the global coordinate frame. Then these two coordinates were differentiated with respect to time to give relationships in terms of velocities and accelerations. Next, a coordinate transformation was performed to provide the relationships in the ball-local coordinate frame. Forces were summed in the ball-local coordinates to allow the unknown quantities to be determined and substituted into Euler's equation. Finally, moments were summed about the ball center and the global origin (point O) to find the desired equations of motion.

Lagrangian analysis was conducted to verify the results from the classical method. After the development of the kinetic and potential energies, construction of the Lagrangian ($L = T - V$), and the appropriate differentiations, the classic results were verified with some manipulations and both were put into standard form. The dynamic equations were found to be:

$$\begin{bmatrix} \bar{I} + m_b \cdot H^2 + J_m + m \cdot R_o^2 + 2 \cdot (H + h_f) \cdot m \cdot R_o + m \cdot (H + h_f)^2 + m \cdot r^2 + J_B & -\frac{J_B}{R_o} - m \cdot R_o - (H + h_f) \cdot m \\ -\frac{J_B}{R_o} - m \cdot R_o - (H + h_f) \cdot m & m + \frac{J_B}{R_o^2} \end{bmatrix} \begin{bmatrix} \ddot{\theta} \\ \ddot{r} \end{bmatrix}$$
$$+ \begin{bmatrix} b + 2 \cdot m \cdot r \cdot \dot{r} & 0 \\ -m \cdot r \cdot \dot{\theta} & C \end{bmatrix} \begin{bmatrix} \dot{\theta} \\ \dot{r} \end{bmatrix} + \begin{bmatrix} -m \cdot g \cdot \left(-r \cos(\theta) + R_o \sin(\theta) + (H + h_f) \sin(\theta) \right) \\ m \cdot g \cdot \sin(\theta) \end{bmatrix} = \begin{bmatrix} \tau \\ 0 \end{bmatrix}$$

The full Maple development of the dynamic equations for both analyses can be found in Appendix A.

Parameter Identification

After developing the governing differential equations, the parameters used in the equations needed to be determined. Some parameters could be determined as derived from easily measured quantities. For example, the mass, diameter, and thickness of the racquetball and coupling collar could all be measured and used to determine the rotational inertias of both parts. To determine the inertia of the beam assembly (beam, cradle, sensor brackets, and sensors), it was modeled in SolidWorks, had appropriate material properties applied, and a solver within SolidWorks was used to determine its rotational inertia.

There were three parameters that proved more difficult to identify. These were the motor inertia, motor friction, and the proportional constant that determines the amplifier output as a function of the input voltage. Due to a lack of documentation for the motor, the motor inertia and motor friction needed to be determined through an experimental procedure of collecting data and determining estimates. The difficulty in obtaining the proportional constant was produced by the unusable current sense channel on the amplifier, a channel that should provide an analog voltage proportional to the current delivered to the motor. The motor model was changed from a current-input model to incorporate the amplifier and became a voltage-input model, to utilize the known voltage information. The transfer function of the motor was assumed to be $\frac{\theta(s)}{I(s)} = \frac{K_t}{J_m \cdot s^2 + b \cdot s}$ where θ is the position of the motor, I is the motor input current, K_t is the motor torque constant, J_m is the motor inertia, and b is the motor viscous friction coefficient. Because of the difficulty encountered in obtaining a measurement of the amplifier output current the substitution of $I = K_v \cdot V$ was used, which relates the amplifier output current to its command voltage. After rearranging the transfer function to use voltage as an input, the multiplied constants are renamed as: $K_v \cdot K_t = \alpha$. With this substitution the motor model became: $\frac{\theta(s)}{V(s)} = \frac{\alpha}{J_m \cdot s^2 + b \cdot s} = \frac{\alpha / J_m}{s^2 + b / J_m \cdot s}$. This can be rearranged to be a model of the motor velocity (instead of position), given by: $\frac{s \cdot \theta(s)}{V(s)} = \frac{\alpha / J_m}{s + b / J_m}$.

With the motor model changes described above, the experiment needed to determine the motor inertia and motor friction could also be used to determine the unknown constant α with the following procedure. First, without any load attached to the motor, a range of known voltages were used as inputs to the system. For each input, the resulting system step response was recorded to determine the time constant and steady-state velocity corresponding to each voltage. Taking the inverse Laplace Transform of the given motor velocity transfer function, it is clear that the time constant of the system is given by $\tau_t = J_m / b$ and the relationship between steady-state velocity and input voltage is given by $\dot{\theta}(t) = (\alpha / b) \cdot V(t)$. This relationship is shown in Figure 3-2. Also illustrated in Figure 3-2 is the static friction that the motor must overcome, which has the effect of making the relationship not strictly linear.

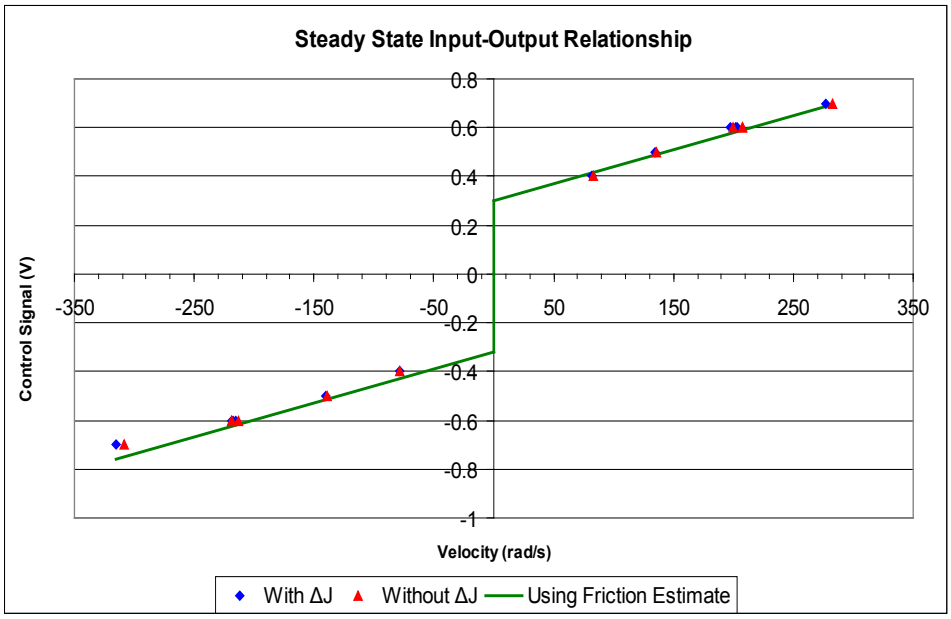

Figure 3-2 Relationship between steady-state velocity and command voltage

After performing an exponential curve-fit to the experimental step-response data and a linear regression applied to the velocity/voltage relationship, estimates for the ratios J_m/b and α/b can be obtained. If a transfer function model for the motor was all that was desired, these would be sufficient. However, the actual motor inertia and the motor friction were needed in the dynamic equations for the system simulation and controller development.

Therefore, a method of determining the specific quantities within the ratios was developed. By adding a known inertia to the motor (ΔJ) and performing the same experimental tests and curve-fits and by examining the difference in time constants, illustrated in Figure 3-3, an estimate of the ratio $\Delta J/b$ could be determined. Then b is easily determined from the known ΔJ, and J_m and α readily determined from the calculated b. The equations in Table 3.1 demonstrate the process.

Table 3.1 Equations used to determine motor coefficient *b*

$\tau_{motor} = \frac{J_m}{b}$	$\tau_{w/\Delta J} = \frac{\Delta J + J_m}{b}$	$\tau_{w/\Delta J} - \tau_{motor} = \frac{\Delta J}{b}$	$b = \frac{\Delta J}{\tau_{w/\Delta J} - \tau_{motor}}$

When performing the experiments, the collar used to connect the motor to the beam assembly was used as ΔJ. Table 3.2 lists the identified parameters and their values for the apparatus used for this work.

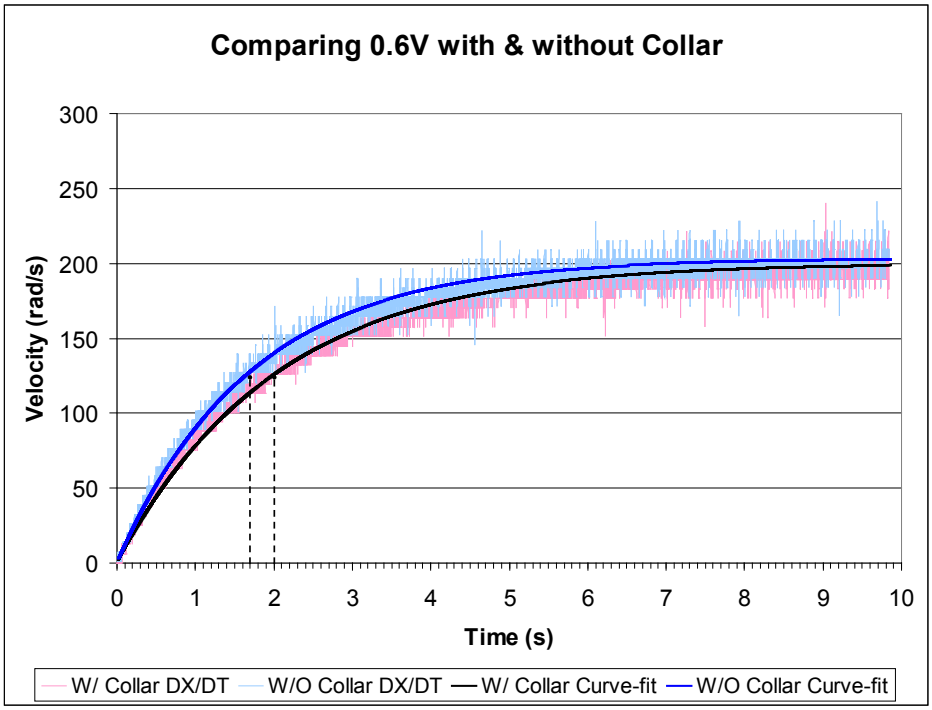

Figure 3-3 Graph of 0.6 Volt Step Responses showing Time Constants

Table 3.2 System Parameter Values

Description	Parameter	Value	Units	Determination
Ball Inertia	J_b	1.844E-05	$kg \cdot m^2$	Calculated
Ball Radius	R_{ball}	2.830E-02	m	Measured
Collar Inertia	ΔJ	3.293E-05	$kg \cdot m^2$	Calculated
Local Acceleration of Gravity	g	9.79987	m/s^2	Research
Modified Torque Constant	α	1.060E-01	$N \cdot m/V$	Experimental
Motor Friction	b	1.484E-04	$N \cdot m \cdot s$	Experimental
Motor Inertia	J_m	2.757E-04	$kg \cdot m^2$	Experimental
Offset Distance	H	2.788E-02	m	Measured
Point of contact offset	h_f	4.100E-03	m	Calculated
Radius of Travel	R_o	2.340E-02	m	Calculated
Rotational Inertia of Beam	$\bar{I}$	2.569E-01	$kg \cdot m^2$	SolidWorks

CHAPTER 4 - Controller

This chapter discusses the control chosen for the ball-and-beam apparatus as well as the implementation of the control algorithm. The control was implemented first in the simplest system simulation as part of an undergraduate Honors Research project.

Control Selection

From the results presented in Chapter 3, it is straightforward to see that the state-space model of the ball-and-beam apparatus is fourth-order. At all points during the parameter identification process it was clear that the ball-and-beam system had one positive, real pole in the *s*-plane and two very lightly damped poles on the $j\omega$-axis. Therefore, the pole placement method of control was selected because it provided the ability to stabilize unstable poles. This method is dependent on the model being fairly accurate, which may have caused some problems during initial tests. In order to accurately simulate the nonlinear system, all of the parameters in the dynamic equations of Chapter 3 needed to be identified. After these parameters had been determined, a system simulation was created in Simulink; its block diagram is included in Appendix B.

To calculate the gains necessary to place the system poles at the desired locations, the dynamic equations were linearized. The linearized equations were found to be:

$$\begin{bmatrix} \bar{I} + m_b \cdot H^2 + J_m + m \cdot R_o^2 + 2 \cdot (H + h_f) \cdot m \cdot R_o + m \cdot (H + h_f)^2 + J_B & -\frac{J_B}{R_o} - m \cdot R_o - (H + h_f) \cdot m \\ -\frac{J_B}{R_o} - m \cdot R_o - (H + h_f) \cdot m & m + \frac{J_B}{R_o^2} \end{bmatrix} \begin{bmatrix} \ddot{\theta} \\ \ddot{r} \end{bmatrix}$$
$$+ \begin{bmatrix} b & 0 \\ 0 & C \end{bmatrix} \begin{bmatrix} \dot{\theta} \\ \dot{r} \end{bmatrix} + \begin{bmatrix} 0 \\ 0 \end{bmatrix} = \begin{bmatrix} \tau \\ 0 \end{bmatrix}$$

The system poles were placed at numerous locations during simulations to determine which set of poles would be most appropriate for the real system, and the final poles were chosen as [-2+2*i*, -2-2*i*, -6, -7]. Using the linearized system equations, the controller gain was found to be: $K = \begin{bmatrix} 27.028773 & -16.678876 & 4.931127 & -13.182346 \end{bmatrix}$. Also, the observer gains were calculated, and the state estimator was included in the simulation; its function is provided in Appendix B. The reasons for using a state estimator are discussed in more detail in Chapter 6. After simulating the system, all of the gains were implemented in the system controller.

Control Implementation

The controller was created using a PC running LabVIEW Real Time with an NI PCIe-6361 X-series multifunction data-acquisition (DAQ) card that allowed communication between the sensors, controller, and amplifier. The real time PC is programmed to run the control loop at 10 kilohertz, which is assumed to be faster than the limiting dynamics of the motor, so that the control loop does not adversely affect the system performance.

The control program initializes all of the necessary communication channels and variables on startup. Then it launches a loop that performs sensor readings, state estimation, control calculation, control output, and data collection. The gains developed in the simulation are used in the controller to create a stable system.

As a safety precaution, and to prevent the sensor wires from getting wrapped around the motor shaft, the control loop automatically stops if the beam angle exceeds 45 degrees. Otherwise, the system will continue operating until the user stops it. The figures in Appendix C show the LabVIEW controller and its initialization. This controller is very similar to a controller developed at Kansas State University for controlling a motor in an undergraduate laboratory setting (Wieneke et al. 384-389).

CHAPTER 5 - Acoustic Sensor Configuration

Prior to installing the acoustic sensors on the beam, a single sensor was purchased and put through preliminary testing to demonstrate that they could sense the position of a ball and also sense the position of a ball as it was rolling. After passing these tests, the apparatus was constructed and another sensor was purchased. However, it became apparent that the ball position was not always being accurately determined because the beam was not able to place the ball in the correct location. This chapter details the different configurations tested and implemented using both acoustic sensors.

End-to-End

This configuration was intended to eliminate the dead zones immediately in front of each sensor. To accomplish this, each sensor would measure the ball's position anywhere on the beam, from its dead zone to the opposite end. Then, a switching algorithm would determine which sensor was giving a correct reading, based on the measured and estimated ball positions. Given what was known about the sensors prior to testing, this configuration made the most sense, but in practice this configuration could not be implemented.

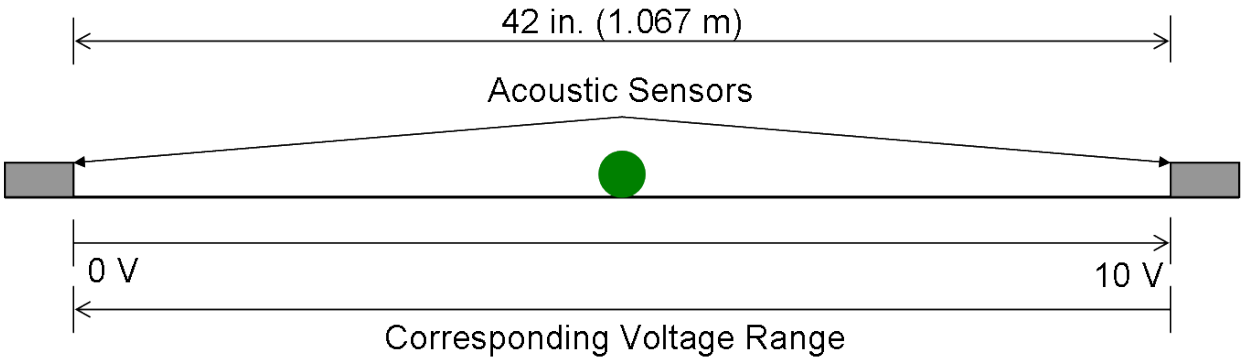

Figure 5-1 End-to-End configuration

While the sensor specifications given in the data sheet appear correct for a larger, flat surface, they are difficult to realize when measuring a smaller, spherical surface. In order for the sensors to measure the ball's position accurately, their gains needed to be turned up rather high, which also limited their range. The shorter range did not allow the sensors to detect the ball at the opposite end of the beam, which meant the configuration needed to be changed. The next

logical configuration was to use each sensor to find the ball's position on half of the beam length, because the ball should not be traveling into the sensor dead zones during normal operation.

End-to-Center

In this configuration each sensor measures the ball position from its dead zone to the center of the beam. The sensor output voltages were configured as illustrated in Figure 5-2. Arranging the voltages this way allowed for adding the two sensor voltages together to determine the ball's position along the entire length of the beam. However, this configuration had some unexpected results.

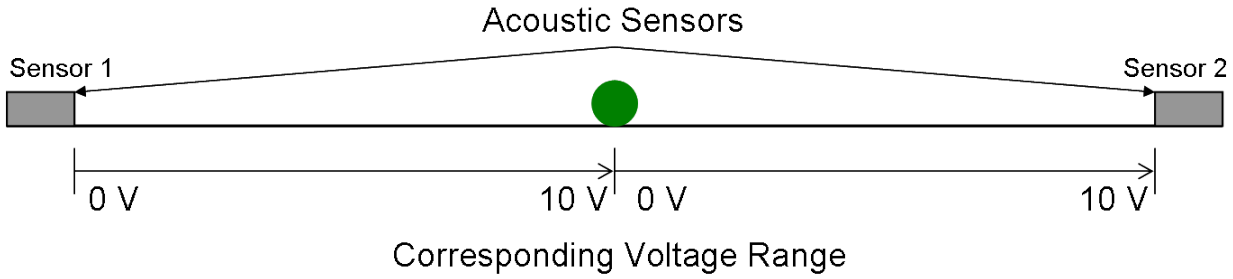

Figure 5-2 End-to-Center configuration

First, with both sensors taking measurements continuously and aimed directly at each other, the ultrasonic waves traveling the length of the beam would interfere with the opposite sensor's measurement. Illustrated in the graph of Figure 5-3 is the sensor interference. The points labeled V1 are the voltage output from the first sensor, V2 is the voltage output from the second sensor plus 10 volts so that it would line up with the ideal linear regression and V3 is the voltage sum from both sensors. The sensor interference is best illustrated by the points that seem coincident with a line possessing negative slope. Ideally, the V1 points above 54.6 centimeters (center of the beam) should all be at 10 volts; similarly with the V2 points below 54.6 centimeters. Then the V3 points would all be along a single line with positive slope.

This interference is not constant, so the sensors do not always provide the documented voltages; the output voltage actually alternates between the ideal linear model and the undesired, negative slope linear model. After this discovery, it became necessary to coordinate the sensor measurements. This was accomplished by establishing sensor one as a master and sensor two as a slave. The master sensor then coordinates alternating measurements with the slave. In this configuration the system performed much better; in fact an accurate linear fit could be developed.

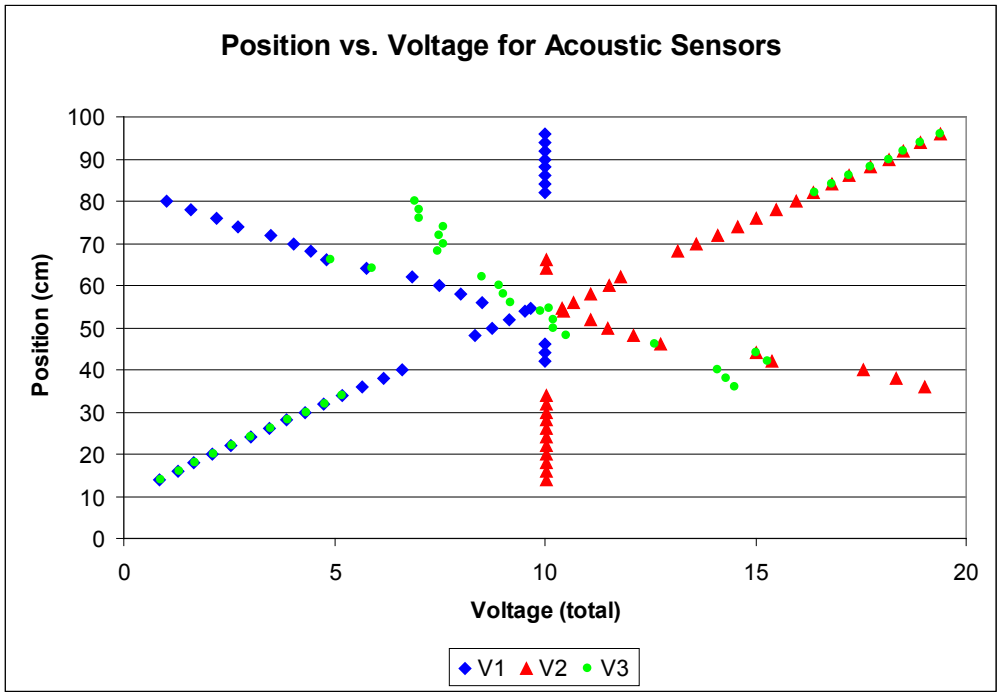

Figure 5-3 Position as a function of Sensor Voltage with interference

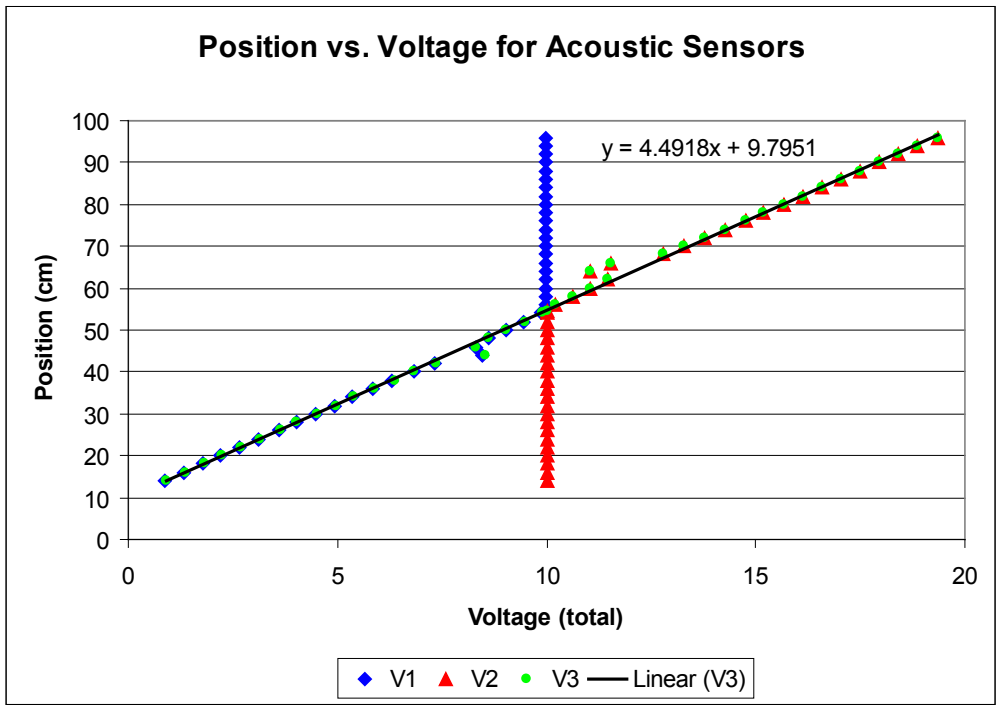

Figure 5-4 Position as a function of Sensor Voltage with V3 linear fit

It can be seen in the graph of Figure 5-4 that even though a linear regression can be performed on the V3 data, there are two locations where small groups of points do not match up

with the trend line. With the sensors alternating measurements, this could not have been caused by interference any longer. Also, these abnormal spots created disturbances in the controller that caused instabilities in the system. After further analysis, it was determined that these unpredictable zones were caused by the target selection; using a larger target, or a target with a non-spherical surface, resulted in reduction of these zones. Once again, the sensor configuration needed to be adjusted.

Overlapping

In order to obtain a reliable measurement of the ball's position as it crossed the abnormal spots within each sensor's range, the ranges of each sensor were expanded to cover the unpredictable zone of the opposite sensor, as illustrated in Figure 5-5. This configuration allows for accurate determination of the ball's position along the length of the beam (excluding the sensor dead zones), and avoided requiring the controller to constantly switch sensors when the ball was in the center of the beam.

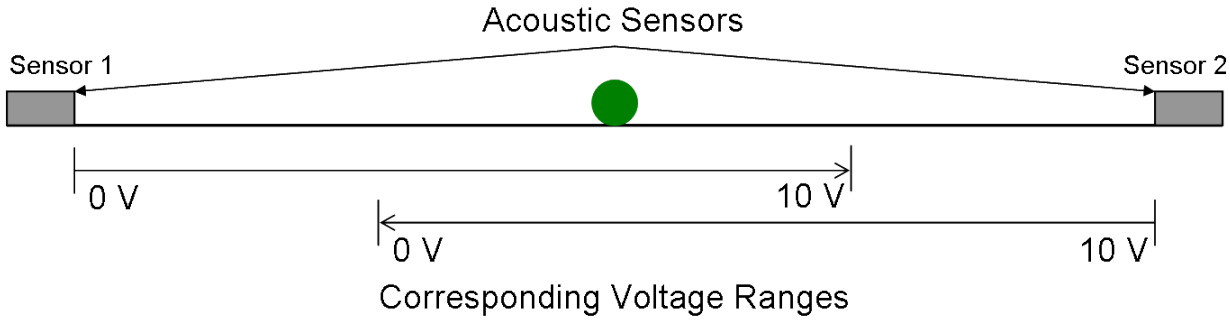

Figure 5-5 Overlapping Range configuration

After implementing the overlapping configuration with the hardware, the results of Figure 5-6 were obtained. As shown, there is a linear position to voltage relationship for each sensor.

The linear regressions shown in Figure 5-6 were used to create a system within the controller that switches between sensors, responding prior to the ball entering the unpredictable zone of each sensor, which allows for accurate determination of the ball position between the two sensor dead zones. The controller is also able to maintain the use of one sensor when the ball is in the center, instead of constantly switching at that position; a benefit that reduces conflicts within the controller.

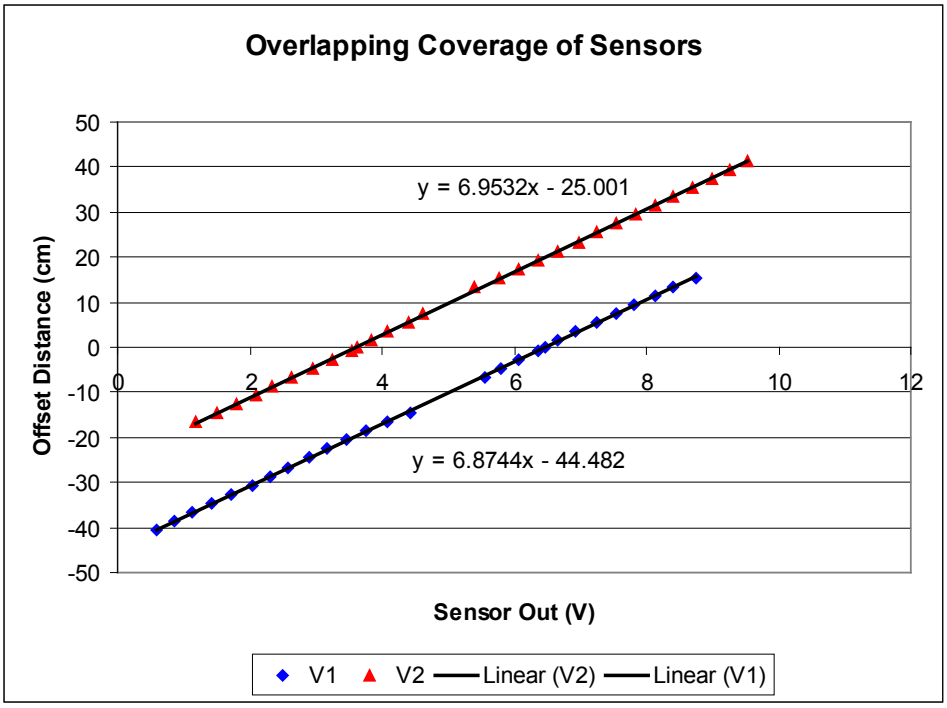

Figure 5-6 Position as function of individual Sensor Voltage

CHAPTER 6 - System Performance

After constructing the system, it needed to be tested to determine if it worked as designed. This chapter describes the process of improving the apparatus so that it controlled the ball position as desired. The system controller runs at 10 kilohertz, which is assumed to be faster than the limiting dynamics present in the motor itself.

Performance Discrepancies

Originally, with a small initial condition the actual system was unstable, while the simulation demonstrated that it should bring the ball to center with ease. This glaring discrepancy launched an attempt to capture more of the actual system's nonlinearities in the simulation. Specifically, the differences in sample rate between the controller, encoder signals, and ultrasonic transducers were included. As mentioned earlier, the controller runs at 10 kilohertz, but the acoustic sensors were found to be running at 20 hertz. Incorporating this difference in the simulation lead to an unstable growth in the ball velocity signal as time progressed because the velocity signal was the discrete derivative of a 20 hertz signal performed at 10 kilohertz. Within the simulation, this was easily corrected by performing the discrete derivative at the same rate as the sensors took measurements. This discovery led to increasing the measurement rate of the ultrasonic sensors to 100 hertz and decreasing the ball velocity discrete derivative rate to 100 hertz.

Increasing Model Accuracy

Seeking an explanation for the performance discrepancies between the simulation and the real system, more of the system nonlinearities were added to the simulation. After incorporating a friction model within the nonlinear system dynamics, the simulation was still not unstable, but it did stabilize the ball to a limit cycle rather than directly to the beam center. This change seemed appropriate, but still needed to be replicated in the actual system, which appeared to be rapidly over-compensating and the ball continued to bounce off of the stops and leave the beam.

One possible explanation for this was inaccuracy in the motor model, because of the need to estimate α and other parameters as described earlier. Therefore the identification tests were performed again after double-checking the amplifier settings and increasing the amplifier reference gain. The results from this second procedure are those presented in Chapter 3. The

only parameter that changed significantly was α, which was largely due to the change in amplifier reference gain.

System Improvement

Changing α did not noticeably improve the system performance, but the system was now making louder audible noises from the motor. Upon examination of the signals from the apparatus, the control signal was found to be saturating. The cause of this was determined to be noisy feedback signals; specifically the feedback velocities, which were determined by using a discrete derivative. With this discovery, the decision was made to implement a state estimator to provide feedback velocities, providing a cleaner signal to the controller.

Using a state estimator led to greatly improved system performance. The ball no longer launched into instability, but often would be stabilized in a small amplitude limit cycle. However, the ball would almost always be stabilized at a point off-center on the beam, instead of the desired center point. It was during these tests that the acoustic sensors were fine-tuned, further stabilizing the system by eliminating false ball positions, reducing the sensor switching when the ball was at the center point of the beam, and providing appropriate coverage of sensor unpredictable zones. Unfortunately, none of these improvements removed the steady-state balancing error of the controller.

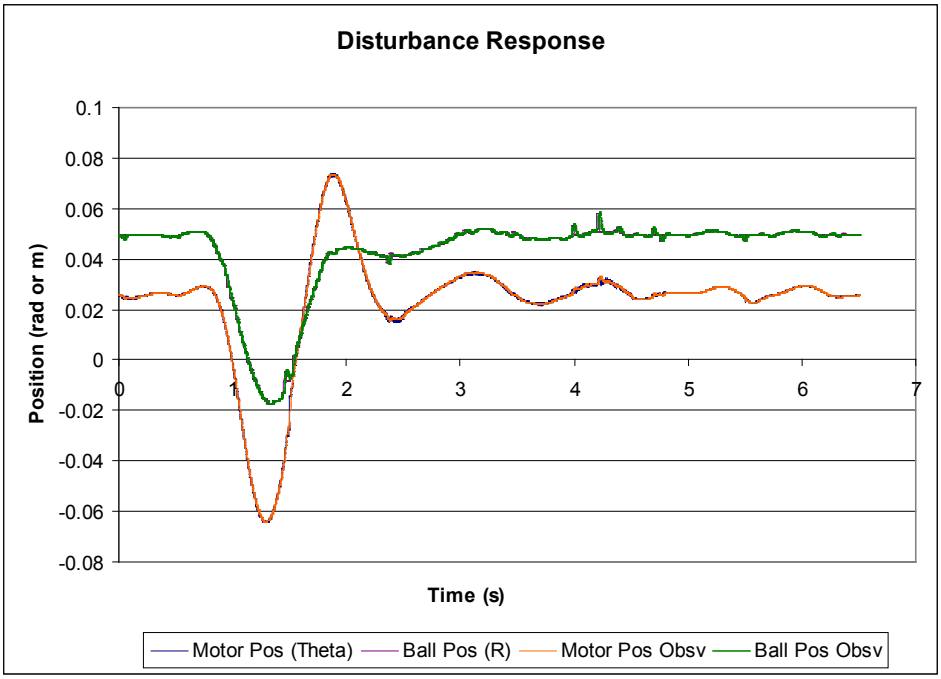

Figure 6-1 Illustration of steady-state error and return after disturbance

Overcoming Static Friction

An observation was made regarding the steady-state ball position error, that it was always in the same location and that it appeared that there was not enough error in the system to cause the control signal to be high enough to drive the ball to zero, the beam center. It was assumed that this behavior was caused by static friction, or stiction, present in the motor that had not been accounted for in the model.

One last addition was then made to the controller, including an anti-stiction capability. The limits of the anti-stiction function were slowly increased, decreasing the steady-state error, until the beam balanced the ball properly in the center with a very small amplitude limit cycle, as illustrated in both Figure 6-2 and Figure 6-3.

With the system balancing the ball in the center from an initial condition, it was tested to see if it would reject disturbances in the ball position and return the ball to center, producing the results shown in Figure 6-4. The ball was disturbed in both directions from center, and each time the controller caused the beam to bring the ball back to center and continue balancing it there.

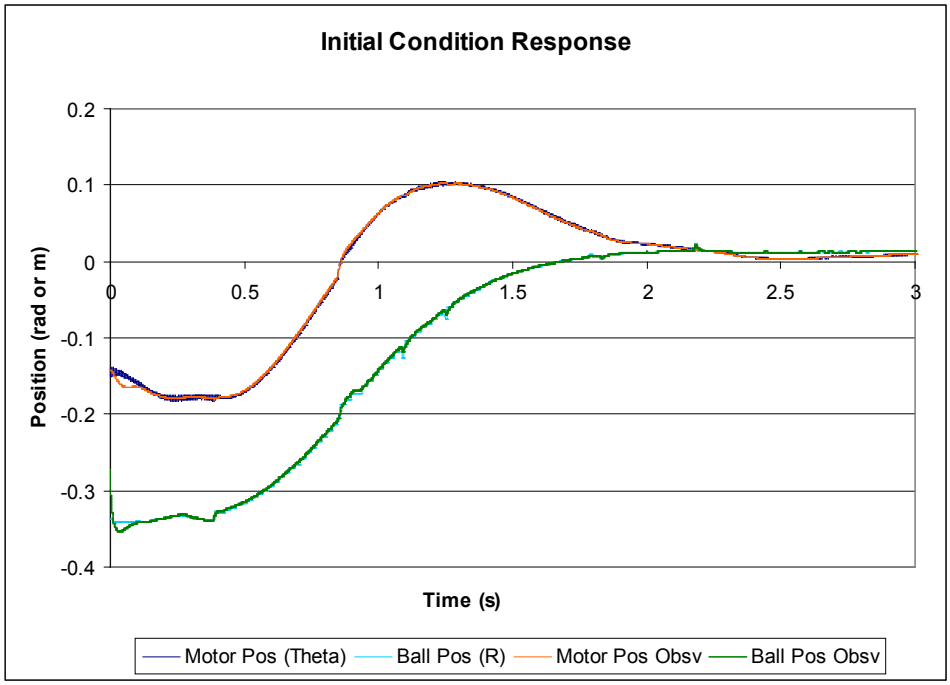

Figure 6-2 Depiction of initial condition response during anti-stiction tuning

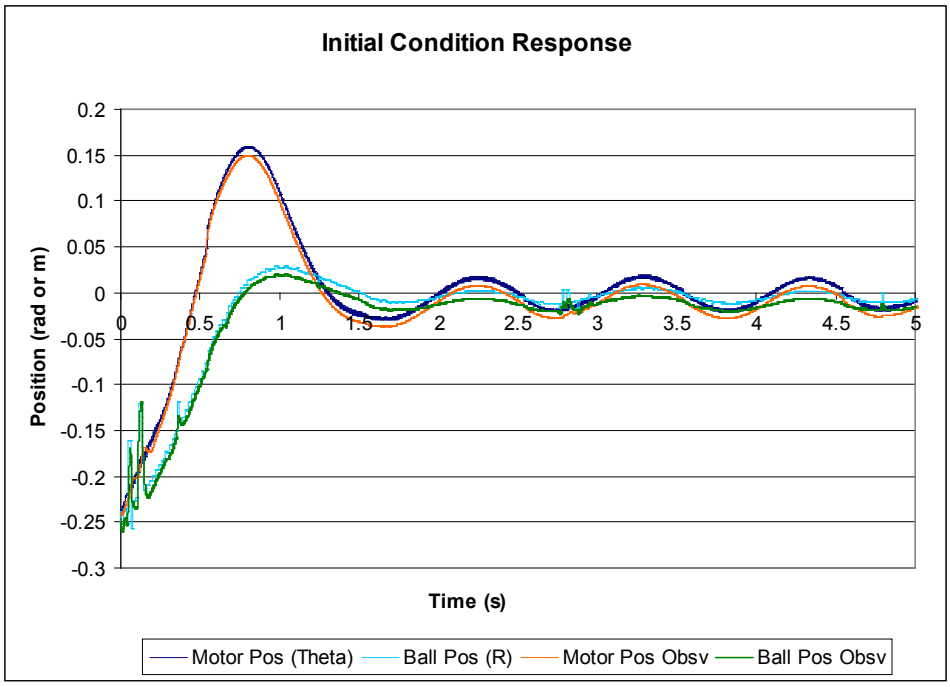

Figure 6-3 Illustration of centered limit cycle

Figure 6-4 Disturbance Response of final system

Demonstration of Robustness

As a demonstration of the robustness of the system controller, a different ball was placed on the beam to determine if the controller could still regulate the ball position with acceptable performance. The other ball is solid plastic and was originally part of an omnidirectional wheel assembly. Figure 6-5 depicts both the racquetball and the plastic ball to illustrate the size difference.

Figure 6-5 Racquetball and plastic ball

A further comparison between the two balls shows differences between their open loop poles, calculated from the linearized system equations. Table 6.1 provides the open loop poles for four linearization cases: racquetball at beam center, racquetball 0.35 meters away from center, plastic ball at beam center, and plastic ball at 0.35 meters away from center. For this demonstration it is worth noting that the open loop poles for the plastic ball are almost 20% greater in magnitude than the open loop poles for the racquetball.

Table 6.1 Open loop pole locations for different scenarios

Ball:	Racquetball		Plastic ball	
Properties:	Mass: 0.0402 kg	Radius: 0.0283 m	Mass: 0.0643 kg	Radius: 0.0247 m
Scenario:	Beam center	0.35 m	Beam center	0.35 m
Poles:	1.6826 -1.6830 -0.0002 + 1.6929i -0.0002 - 1.6929i	1.6748 -1.6751 -0.0002 + 1.6849i -0.0002 - 1.6849i	2.0054 -2.0057 -0.0002 + 2.0256i -0.0002 - 2.0256i	1.9906 -1.9909 -0.0002 + 2.0103i -0.0002 - 2.0103i

The controller successfully stabilized the smaller ball and also rejected disturbances to the plastic ball's position; the disturbance rejection to separate disturbances of opposite polarity,

which occur at approximately 0.75 seconds and 4 seconds, is shown in Figure 6-6. The noise on the ball's position in Figure 6-6 is from the ultrasonic sensors' difficulty in measuring the smaller ball's position.

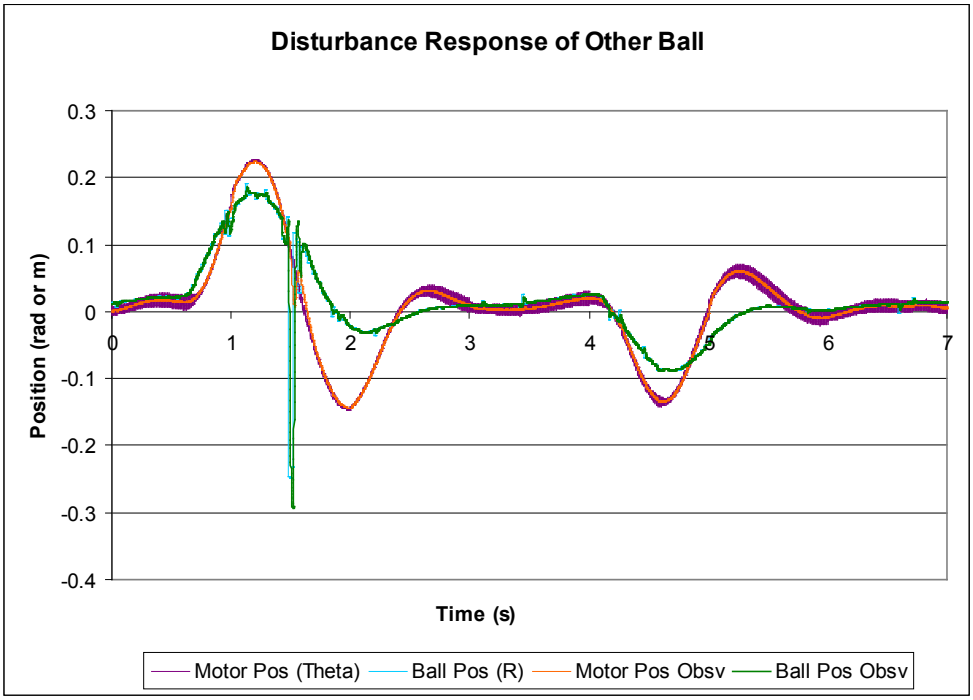

Figure 6-6 Disturbance Response of final system with other ball

CHAPTER 7 - Conclusions

The purpose of this investigation was to determine the feasibility of using ultrasonic sensors to determine the position of a ball so that it could be balanced on a beam and also to specify the equipment and configuration to give this ball-and-beam system wireless capability. This chapter will show that these goals have been met and provide the author's conclusions about the project.

Wireless Capability

In Chapter 2 details were provided about specific pieces of equipment that could be combined with the current system to remove the hardwired connection of the sensors and control output from the controlling real time PC. Using those recommendations, and the configuration illustrated in Figure 2-2, the ball-and-beam apparatus used for this work could become wireless. This would effectively remove the columns for the NI CB-68LPR and NI PCIe-6361 in Table 2.1 and add columns for the extra circuitry, the NI WLS-9205, and the two NI WLS-9472 units. In order to complete this process the items listed in Table 7.1 should be considered for purchase or construction. Only one NI WLS-9472 is listed for purchase because one unit is already available for use.

Table 7.1 Items needed to implement wireless capability

Item	Purpose
Digital to Analog Converter	Converts digital out signal to analog voltage for amplifier
NI WLS-9205	Allows analog input of acoustic sensors
NI WLS-9472	Provides 8 digital out channels
Quadrature Decoding Circuit	Determines position from motor encoder and outputs a 16-bit number
Wireless Router	Allows communication with the NI Wireless DAQs

Acoustic Sensor Usage

The Senix acoustic sensors selected for this project were able to be configured for use in this ball-and-beam application, as detailed in Chapter 5. After some testing and tweaking of parameters, the sensors worked very well, measuring the ball's position accurately so that it could be balanced in the center of the beam by the controller. This was described in Chapter 6,

with the included performance improvement of adding the anti-stiction capability to the controller. These sensors performed well for this work and demonstrated that acoustic sensors are a viable alternative to other methods of determining the ball's position.

References

Advanced Motion Controls. "Analog Servo Drive." Advanced Motion Control. 10/29/2009. <http://www.a-m-c.com/download/datasheet/be25a20ac.pdf>.

Ito, Bennett T. Stabilizing the Ball on Beam System with Analog Feedback. Bachelor of Science Massachusetts Institute of Technology, 2004.

National Instruments Corporation. "**NI WLS-9205**." National Instruments Corporation. a. <http://sine.ni.com/nips/cds/view/p/lang/en/nid/207479>.

---. "**NI WLS-9472**." National Instruments Corporation. b. <http://sine.ni.com/nips/cds/view/p/lang/en/nid/206856>.

Quanser Inc. "Rotary Control Challenge." Quanser Inc. <http://www.quanser.com/english/html/challenges/fs_chall_rotary_flash.htm>.

Rosales, Evencio A. A Ball-on-Beam Project Kit. Bachelor of Science Massachusetts Institute of Technology, 2004.

Rosales, E. A., et al. "An Open-Ended Ball-Balancing Laboratory Project for Undergraduates." American Control Conference (ACC), 2004. .

Senix Corporation. "ToughSonic TSPC Series." Senix Corporation. <http://www.senix.com/family_tspc.htm>.

Sheng, Jansen, Jay Renner and William S. Levine. "A Ball and Curved Offset Beam Experiment." American Control Conference (ACC), 2010.

Situm, Zeljko. "A Pneumatically Actuated Ball and Beam System." International Journal of Mechanical Engineering Education 36.3 (2008): 225-34.

Wieneke, Jacob, et al. "Redesign of an Undergraduate Controls Laboratory with an Eye Toward Accommodating Future Upgrades." American Control Conference (ACC), 2010.

Appendix A - Dynamic Equations Development

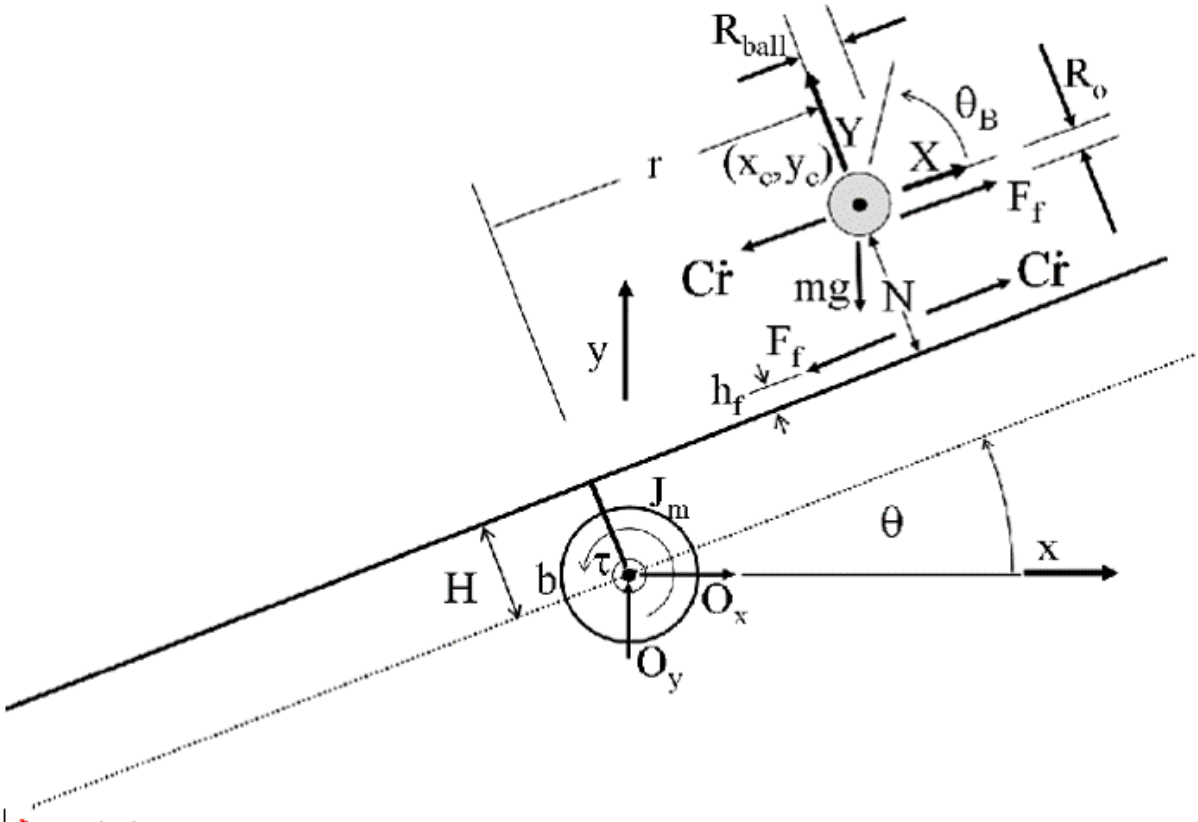


```
> restart :
> with(linalg) :
> #Ball Kinematics in Global Frame
> x[C] := r·cos(θ) - R[o]·sin(θ) - (H + h[f])·sin(θ);
```

$$x_C := r\cos(\theta) - R_o\sin(\theta) - (H + h_f)\sin(\theta) \tag{1}$$

```
> xdot[C] := diff(x[C], r) * Dr + diff(x[C], θ) * Dtheta;
```

$$xdot_C := \cos(\theta)\, Dr + \left(-r\sin(\theta) - R_o\cos(\theta) - (H + h_f)\cos(\theta)\right) Dtheta \tag{2}$$

```
> xddot[C] := simplify(diff(xdot[C], r) * Dr + diff(xdot[C], θ) * Dtheta + diff(xdot[C], Dr)
      * DDr + diff(xdot[C], Dtheta) * DDtheta);
```

$$xddot_C := -2\sin(\theta)\, Dtheta\, Dr - Dtheta^2\, r\cos(\theta) + Dtheta^2\, R_o\sin(\theta) + Dtheta^2\sin(\theta)\, H + Dtheta^2\sin(\theta)\, h_f + \cos(\theta)\, DDr - DDtheta\, r\sin(\theta) - DDtheta\, R_o\cos(\theta) - DDtheta\cos(\theta)\, H - DDtheta\cos(\theta)\, h_f \tag{3}$$

```
> y[C] := r*sin(θ) + R[o]*cos(θ) + (H + h[f])·cos(θ);
```

$$y_C := r\sin(\theta) + R_o\cos(\theta) + (H + h_f)\cos(\theta) \tag{4}$$

```
> ydot[C] := diff(y[C], r) * Dr + diff(y[C], θ) * Dtheta;
```

(5)

$$ydot_C := \sin(\theta)\, Dr + \left(r\cos(\theta) - R_o \sin(\theta) - (H + h_f)\sin(\theta)\right) Dtheta \tag{5}$$

```
> yddot[C] := simplify(diff(ydot[C], r) * Dr + diff(ydot[C], θ) * Dtheta + diff(ydot[C], Dr)
      * DDr + diff(ydot[C], Dtheta) * DDtheta);
```

$$yddot_C := 2\cos(\theta)\, Dtheta\, Dr - Dtheta^2 r \sin(\theta) - Dtheta^2 R_o \cos(\theta) - Dtheta^2 \cos(\theta)\, H - Dtheta^2 \cos(\theta)\, h_f + \sin(\theta)\, DDr + DDtheta\, r\cos(\theta) - DDtheta\, R_o \sin(\theta) - DDtheta \sin(\theta)\, H - DDtheta \sin(\theta)\, h_f \tag{6}$$

```
> #Ball Kinematics in Local Frame
> Xddot[C] := simplify(xddot[C]*cos(θ) + yddot[C]*sin(θ));
```

$$Xddot_C := -Dtheta^2 r + DDr - DDtheta\, R_o - DDtheta\, H - DDtheta\, h_f \tag{7}$$

```
> Yddot[C] := simplify(-xddot[C]*sin(θ) + yddot[C]*cos(θ));
```

$$Yddot_C := 2\, Dtheta\, Dr - Dtheta^2 H - Dtheta^2 h_f + DDtheta\, r - Dtheta^2 R_o \tag{8}$$

```
> Xdot[C] := simplify(xdot[C]*cos(θ) + ydot[C]*sin(θ));
```

$$Xdot_C := Dr - Dtheta\, R_o - Dtheta\, H - Dtheta\, h_f \tag{9}$$

```
> Ydot[C] := simplify(-xdot[C]*sin(θ) + ydot[C]*cos(θ));
```

$$Ydot_C := Dtheta\, r \tag{10}$$

```
> #Sum of forces in ball radial direction
> SFr := expand(simplify((F[f]-C*Dr) - m*g*sin(θ) - m*Xddot[C]));
```

$$SFr := F_f - C\, Dr - m\, g \sin(\theta) + m\, Dtheta^2 r - m\, DDr + m\, DDtheta\, R_o + m\, DDtheta\, H + m\, DDtheta\, h_f \tag{11}$$

```
> F[f] := expand(solve(SFr = 0, F[f]));
```

$$F_f := C\, Dr + m\, g \sin(\theta) - m\, Dtheta^2 r + m\, DDr - m\, DDtheta\, R_o - m\, DDtheta\, H - m\, DDtheta\, h_f \tag{12}$$

```
> #Sum of moments on Ball about mass center
> SMB := R[o]*F[f]-J[B]*(DDtheta-DDr/R[o]);
```

$$SMB := R_o \left(C\, Dr + m\, g \sin(\theta) - m\, Dtheta^2 r + m\, DDr - m\, DDtheta\, R_o - m\, DDtheta\, H - m\, DDtheta\, h_f\right) - J_B \left(DDtheta - \frac{DDr}{R_o}\right) \tag{13}$$

```
> SMB := expand(SMB/R[o]);
```

$$SMB := C\, Dr + m\, g \sin(\theta) - m\, Dtheta^2 r + m\, DDr - m\, DDtheta\, R_o - m\, DDtheta\, H - m\, DDtheta\, h_f - \frac{J_B\, DDtheta}{R_o} + \frac{J_B\, DDr}{R_o^2} \tag{14}$$

```
> #Sum of forces on ball in the transverse
```

direction

```
> SFtheta := expand(simplify(N - m*g*cos(θ) - m*Yddot[C]));
```

$$SFtheta := N - m\,g\cos(\theta) - 2\,m\,Dtheta\,Dr + m\,Dtheta^2\,H + m\,Dtheta^2\,h_f - m\,DDtheta\,r + m\,Dtheta^2\,R_o \tag{15}$$

```
> N := expand(simplify(solve(SFtheta = 0, N)));
```

$$N := m\,g\cos(\theta) + 2\,m\,Dtheta\,Dr - m\,Dtheta^2\,H - m\,Dtheta^2\,h_f + m\,DDtheta\,r - m\,Dtheta^2\,R_o \tag{16}$$

```
> #Sum of moments around origin (center of rotationg shaft)
> MSO := -expand(simplify(-r*N - (H + h[f])·C*Dr + τ + (F[f])·(H + h[f]) - (Ibar + m_b·H^2 + J_m)*DDtheta) + SMB·R[o] - b·Dtheta);
```

$$MSO := m\,DDtheta\,r^2 + m\,DDtheta\,H^2 + m\,DDtheta\,h_f^2 - m\,DDr\,h_f + DDtheta\,m_b\,H^2 - m\,DDr\,H - \tau - R_o\,m\,g\sin(\theta) + 2\,r\,m\,Dtheta\,Dr + b\,Dtheta + 2\,m\,DDtheta\,R_o\,H + DDtheta\,Ibar + 2\,m\,DDtheta\,H\,h_f + 2\,m\,DDtheta\,R_o\,h_f + DDtheta\,J_m - m\,g\sin(\theta)\,H - m\,g\sin(\theta)\,h_f + r\,m\,g\cos(\theta) + m\,DDtheta\,R_o^2 - R_o\,m\,DDr - R_o\,C\,Dr + J_B\,DDtheta - \frac{J_B\,DDr}{R_o} \tag{17}$$

```
> #MSO includes the addition of zero through adding SMB*R[o] to get a symmetric mass matrix
> massNE := matrix(2, 2, [simplify(coeff(MSO, DDtheta)), (coeff(MSO, DDr)), (coeff(SMB, DDtheta)), coeff(SMB, DDr)]);
```

$$massNE := \begin{bmatrix} m\,r^2 + m\,H^2 + m\,h_f^2 + m_b\,H^2 + 2\,m\,R_o\,H + Ibar + 2\,m\,H\,h_f + 2\,m\,R_o\,h_f + J_m + m\,R_o^2 + J_B, & -m\,h_f - m\,H - R_o\,m - \frac{J_B}{R_o} \\ -m\,h_f - m\,H - R_o\,m - \frac{J_B}{R_o}, & m + \frac{J_B}{R_o^2} \end{bmatrix} \tag{18}$$

```
> Gne := matrix(2, 1, [expand(coeff(MSO, g)·g), simplify(coeff(SMB, g))·g]);
```

$$Gne := \begin{bmatrix} -R_o\,m\,g\sin(\theta) - m\,g\sin(\theta)\,H - m\,g\sin(\theta)\,h_f + r\,m\,g\cos(\theta) \\ m\,g\sin(\theta) \end{bmatrix} \tag{19}$$

```
> Cne := matrix(2, 2, [simplify(coeff(MSO, Dtheta)), simplify(coeff(coeff(MSO + (SMB·R[o]), Dr)·Dr - coeff(MSO + (SMB·R[o]), Dtheta)·Dtheta, Dr)), expand(coeff(SMB, Dtheta^2)·Dtheta), coeff(SMB, Dr)]);
```

(20)

$$Cne := \begin{bmatrix} 2\,r\,m\,Dr + b & 0 \\ -r\,m\,Dtheta & C \end{bmatrix} \tag{20}$$

```
> #The Cne matrix needed a 2nd zero of SMB*R[o] added to
  MSO to get correct (1,2) term
>
> #Lagrange Analysis
> #Kinetic Energy
> T := 1/2*(Ibar + m_b·H^2 + J_m)*Dtheta^2 + 1/2*J[B]*(-Dr/R[o] + Dtheta)^2 + 1/2
      *m*(Xdot[C]^2 + Ydot[C]^2);
```

$$T := \frac{1}{2}\left(Ibar + m_b H^2 + J_m\right) Dtheta^2 + \frac{1}{2} J_B \left(-\frac{Dr}{R_o} + Dtheta\right)^2 + \frac{1}{2} m \left(\left(Dr - Dtheta\,R_o - Dtheta\,H - Dtheta\,h_f\right)^2 + Dtheta^2 r^2\right) \tag{21}$$

```
> #Potential Energy
> V := m*g*(y[C]);
```

$$V := m\,g\left(r\sin(\theta) + R_o\cos(\theta) + (H + h_f)\cos(\theta)\right) \tag{22}$$

```
> L := T - V;
```

$$L := \frac{1}{2}\left(Ibar + m_b H^2 + J_m\right) Dtheta^2 + \frac{1}{2} J_B \left(-\frac{Dr}{R_o} + Dtheta\right)^2 + \frac{1}{2} m \left(\left(Dr - Dtheta\,R_o - Dtheta\,H - Dtheta\,h_f\right)^2 + Dtheta^2 r^2\right) - m\,g\left(r\sin(\theta) + R_o\cos(\theta) + (H + h_f)\cos(\theta)\right) \tag{23}$$

```
> #Differentiate w.r.t. 'theta' direction
> DLDDtheta := diff(L, Dtheta);
```

$$DLDDtheta := \left(Ibar + m_b H^2 + J_m\right) Dtheta + J_B \left(-\frac{Dr}{R_o} + Dtheta\right) + \frac{1}{2} m \left(2\left(Dr - Dtheta\,R_o - Dtheta\,H - Dtheta\,h_f\right)\left(-R_o - H - h_f\right) + 2\,Dtheta\,r^2\right) \tag{24}$$

```
> eq[θ] := simplify(diff(DLDDtheta, r)*Dr + diff(DLDDtheta, Dr)*DDr
      + diff(DLDDtheta, θ)*Dtheta + diff(DLDDtheta, Dtheta)*DDtheta - diff(L, θ)) - τ;
```

$$eq_\theta := -\frac{1}{R_o}\left(-2\,r\,m\,Dtheta\,Dr\,R_o + DDr\,J_B + DDr\,m\,R_o^2 + DDr\,m\,R_o\,H + DDr\,m\,R_o\,h_f - DDtheta\,R_o\,m\,r^2 - DDtheta\,R_o\,m\,H^2 - DDtheta\,R_o\,m\,h_f^2 - DDtheta\,R_o\,m_b H^2 - 2\,DDtheta\,R_o^2\,m\,H - DDtheta\,R_o\,Ibar - 2\,DDtheta\,R_o\,m\,H\,h_f - 2\,DDtheta\,R_o^2\,m\,h_f - DDtheta\,R_o\,J_m - DDtheta\,R_o^3\,m - DDtheta\,R_o\,J_B - m\,g\,R_o\,r\cos(\theta) + m\,g\,R_o^2\sin(\theta) + m\,g\,R_o\sin(\theta)\,H + m\,g\,R_o\sin(\theta)\,h_f\right) - \tau \tag{25}$$

```
> #Differentiate w.r.t. 'r' direction
```

```
> DLDDr := diff(L, Dr);
```

$$DLDDr := -\frac{J_B\left(-\frac{Dr}{R_o} + Dtheta\right)}{R_o} + \frac{1}{2}\,m\left(2\,Dr - 2\,Dtheta\,R_o - 2\,Dtheta\,H - 2\,Dtheta\,h_f\right) \tag{26}$$

```
> eq[r] := simplify(expand(diff(DLDDr, r) * Dr + diff(DLDDr, Dr) * DDr + diff(DLDDr, θ)
      * Dtheta + diff(DLDDr, Dtheta) * DDtheta - diff(L, r))) + C * Dr;
```

$$eq_r := \frac{1}{R_o^2}\left(DDr\,m\,R_o^2 + DDr\,J_B - DDtheta\,R_o^2\,m\,h_f - DDtheta\,R_o^2\,m\,H - DDtheta\,R_o^3\,m\right. \tag{27}$$
$$\left. - DDtheta\,R_o\,J_B - m\,Dtheta^2\,r\,R_o^2 + m\,g\,R_o^2\sin(\theta)\right) + C\,Dr$$

```
> eq[θ] := eval(eq[θ]);
```

$$eq_\theta := -\frac{1}{R_o}\left(-2\,r\,m\,Dtheta\,Dr\,R_o + DDr\,J_B + DDr\,m\,R_o^2 + DDr\,m\,R_o\,H + DDr\,m\,R_o\,h_f\right. \tag{28}$$
$$- DDtheta\,R_o\,m\,r^2 - DDtheta\,R_o\,m\,H^2 - DDtheta\,R_o\,m\,h_f^2 - DDtheta\,R_o\,m_b\,H^2$$
$$- 2\,DDtheta\,R_o^2\,m\,H - DDtheta\,R_o\,Ibar - 2\,DDtheta\,R_o\,m\,H\,h_f - 2\,DDtheta\,R_o^2\,m\,h_f$$
$$- DDtheta\,R_o\,J_m - DDtheta\,R_o^3\,m - DDtheta\,R_o\,J_B - m\,g\,R_o\,r\cos(\theta) + m\,g\,R_o^2\sin(\theta)$$
$$\left. + m\,g\,R_o\sin(\theta)\,H + m\,g\,R_o\sin(\theta)\,h_f\right) - \tau$$

```
> eq[r] := eval(eq[r]);
```

$$eq_r := \frac{1}{R_o^2}\left(DDr\,m\,R_o^2 + DDr\,J_B - DDtheta\,R_o^2\,m\,h_f - DDtheta\,R_o^2\,m\,H - DDtheta\,R_o^3\,m\right. \tag{29}$$
$$\left. - DDtheta\,R_o\,J_B - m\,Dtheta^2\,r\,R_o^2 + m\,g\,R_o^2\sin(\theta)\right) + C\,Dr$$

```
> simplify(coeff(eq[θ], DDtheta)) * DDtheta + simplify(coeff(eq[θ], DDr)) * DDr
      + simplify(coeff(eq[θ], Dtheta)) * Dtheta + coeff(eq[θ], cos(θ)) * cos(θ)
      + simplify(coeff(eq[θ], sin(θ))) * sin(θ) - τ;
```

$$\left(m\,r^2 + m\,H^2 + m\,h_f^2 + m_b\,H^2 + 2\,m\,R_o\,H + Ibar + 2\,m\,H\,h_f + 2\,m\,R_o\,h_f + J_m + m\,R_o^2\right. \tag{30}$$
$$\left. + J_B\right)\,DDtheta - \frac{\left(J_B + m\,R_o^2 + m\,R_o\,H + m\,R_o\,h_f\right)\,DDr}{R_o} + 2\,r\,m\,Dtheta\,Dr$$
$$+ r\,m\,g\cos(\theta) - m\,g\,\left(R_o + H + h_f\right)\sin(\theta) - \tau$$

```
> simplify(coeff(eq[r], DDtheta)) * DDtheta + coeff(eq[r], DDr) * DDr + coeff(eq[r], Dtheta
      ^2) * Dtheta^2 + coeff(eq[r], sin(θ)) * sin(θ) + C·Dr;
```

$$-\frac{\left(J_B + m\,R_o^2 + m\,R_o\,H + m\,R_o\,h_f\right)\,DDtheta}{R_o} + \frac{\left(m\,R_o^2 + J_B\right)\,DDr}{R_o^2} - m\,Dtheta^2\,r + m\,g\sin(\theta) \tag{31}$$
$$+ C\,Dr$$

```
> mass := matrix(2, 2, [simplify(coeff(eq[θ], DDtheta)), expand(coeff(eq[θ], DDr)),
      expand(coeff(eq[r], DDtheta)), expand(coeff(eq[r], DDr))]);
```

$$mass := \begin{bmatrix} m\,r^2 + m\,H^2 + m\,h_f^2 + m_b\,H^2 + 2\,m\,R_o\,H + Ibar + 2\,m\,H\,h_f + 2\,m\,R_o\,h_f + J_m + m\,R_o^2 & \cdots \end{bmatrix} \tag{32}$$

$$+J_B \left[-m h_f - m H - R_o m - \frac{J_B}{R_o}, m + \frac{J_B}{R_o^2} \right] \Bigg]$$

```
> Cmatrix := matrix(2, 2, [b + simplify(coeff(eq[θ], Dtheta)), 0, -m*r*Dtheta, C]);
```

$$Cmatrix := \begin{bmatrix} 2\,r\,m\,Dr + b & 0 \\ -r\,m\,Dtheta & C \end{bmatrix} \tag{33}$$

```
> G = matrix(2, 1, [expand(coeff(eq[θ], g)·g), simplify(coeff(eq[r], g))·g]);
```

$$G = \begin{bmatrix} -R_o\,m\,g\,\sin(\theta) - m\,g\,\sin(\theta)\,H - m\,g\,\sin(\theta)\,h_f + r\,m\,g\,\cos(\theta) \\ m\,g\,\sin(\theta) \end{bmatrix} \tag{34}$$

```
> F = matrix(2, 1, [τ, 0]);
```

$$F = \begin{bmatrix} \tau \\ 0 \end{bmatrix} \tag{35}$$

Appendix B - System Simulation and Gain Calculation Files

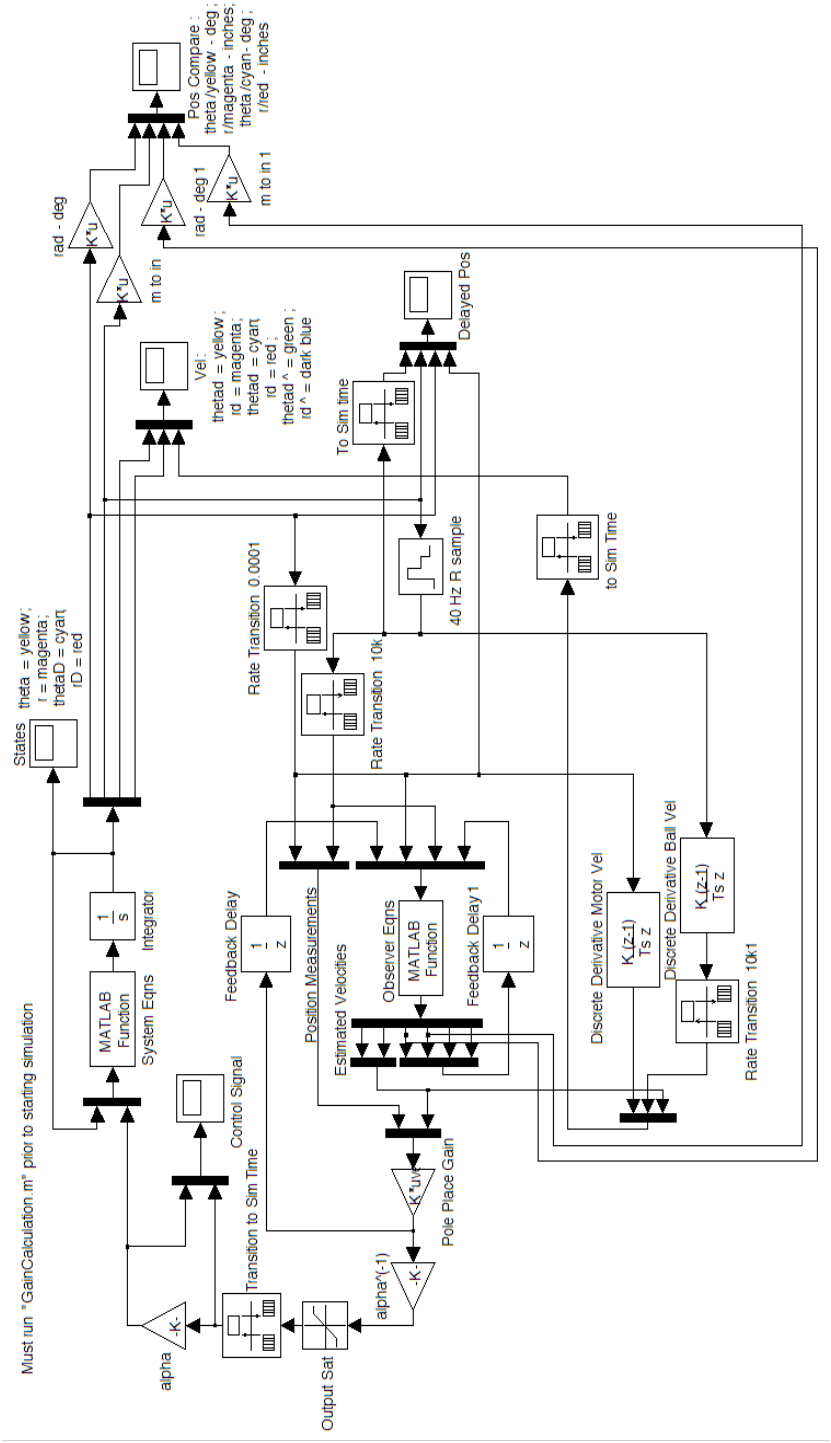

Figure B-1 Simulink simulation block diagram

```
% GainCalculation.m
clear all

% Variable Input
m = 0.0402; %kg (mass of ball)
mb = 1.53767813; %kg (mass of beam)
H = 0.0278765; %m (offset distance)
hf = 4.1/1000; %m (distance from pole of sphere to latitude line of rotation)
% Do = 0.0563626; %m (radius of ball)
Rball = 0.02830; %m (radius of ball)
Ro = 0.0234; %m (radius of travel)
Ibar = 0.25691795825; %kg*m^2 (moment of inertia about center of rot.)
% Ibar = 0.543266; %kg*m^2 (calculated moment of inertia)
% Jb = 0.00001863824; %kg*m^2 (calculated inertia for hollow ball)
Jb = 1.844235466666667e-005; %kg*m^2 (calculated inertia for hollow ball)
% Jb = 0.000138035; %kg*m^2 (calculated inertia for stainless steel ball)
Jc = 3.292554795127158e-005;  %kg*m^2  (collar inertia)
Jm = 0.000275691 + Jc; %kg*m^2 (from Excel Calculations)
bm = 0.000148379; %N*m*s or kg*m^2/s (from Excel Calculations)
alpha = 0.105984964; %N*m/V {Torque constant} (from Excel Calculations)
g = 9.79987; %m/s^2 (specific gravity)
C = .00001; %(assume viscous friction of the ball is negligible)

% Linearized Maple Matrices
Mass = [Ibar + mb*H^2 + Jm + m*Ro^2 + 2*(H+hf)*m*Ro + m*(H+hf)^2 + Jb,
(-1)*((H+hf)*m + (m*Ro + Jb/Ro));
        (-1)*((H+hf)*m + (m*Ro + Jb/Ro)),(m + Jb/(Ro^2))];

Cmatrix = [bm, 0; 0, C];

G = [0; 0];
Gbar = [(-H*m*g-Ro*m*g), m*g; m*g,0];

format long
% Creation of State Space Matrices
F = [0,0,1,0;0,0,0,1; -inv(Mass)*Gbar ,-inv(Mass)*Cmatrix];
G = [0;0;(inv(Mass)*[1;0] )]
H = [1 0 0 0; 0 1 0 0];

% Controller gains
P = [-2+2i,-2-2i,-6,-7];
K=place(F,G,P)

%Observer Calculations
P1=[-50,-51,-52,-53];
L=(place(F',H',P1))'
E=F-L*H

format short
```

```
function DX = fcn(X)

DX = [zeros(4,1)];
% Variable Input
m = 0.0402; %kg (mass of ball)
mb = 1.53767813; %kg (mass of beam)
H = 0.0278765; %m (offset distance)
hf = 4.1/1000; %m (distance from pole of sphere to latitude line of rotation)
% Do = 0.0563626; %m (ball diameter)
Rball = 0.02830; %m (radius of ball)
Ro = 0.0234; %m (radius of travel)
Ibar = 0.25691795825; %kg*m^2 (I about center of rot.)
Jb = 1.844235466666667e-005; %kg*m^2 (calculated inertia for hollow ball)

% slightly different than gain calculation numbers
Jc = 3.2921961e-5;  %kg*m^2
Jm = 0.000275691 + Jc; %kg*m^2 (from Excel Calculations)
bm = 0.000148379; %N*m*s or kg*m^2/s (from Excel Calculations)
g = 9.79987; %m/s^2
C = 0; %(the viscous friction on the ball should be negligible)

% Input X has state vars
theta = X(1);
r = X(2);
Dtheta = X(3);
Dr = X(4);
u= X(5);

% Maple Matrices -- not linearized
Mass= [Ibar + mb*H^2 + Jm + m*Ro^2 + 2*(H+hf)*m*Ro + m*(H+hf)^2 + m*r^2 + Jb,
(-1)*((H+hf)*m + (m*Ro + Jb/Ro));
        (-1)*((H+hf)*m + (m*Ro + Jb/Ro)),(m + Jb/(Ro^2))];

Cmatrix = [bm + 2*r*m*Dr, 0; -r*m*Dtheta, C];

G = [r*m*g*cos(theta)-(H+hf)*m*g*sin(theta)-Ro*m*g*sin(theta);
m*g*sin(theta)];

DDTH(1:2,1) = -inv(Mass)*G -inv(Mass)*Cmatrix*[Dtheta; Dr] +inv(Mass)*[u;0];
DDtheta = DDTH(1,1);
DDr = DDTH(2,1);

%simulation of motor static friction
limitV = 0.25; %any |u| < limitV will not be enough to move motor
limit_dth = 0.2*(2*pi);  %rad/sec
M = -0.0000015; %slope of acceleration motor

if ((abs(u) < limitV) && (abs(Dtheta) < limit_dth))
    DDtheta = M*sign(Dtheta);
end

% Now create State Space Matrices
DX(1,1) = Dtheta;
DX(2,1) = Dr;
DX(3:4,1) = [DDtheta; DDr];
```

```
function VEL = velobsrv(x)

%dT is based on control loop rate
dT=1e-4;

%Observer State Space Matrices -- Calculated in "GainCalculation.m"
G=[0;0; 3.863562657658950; 0.150493329058147];

L = 1.0e+003 *[0.104603612547061  -0.002171658580328
  -0.000340017609210   0.101395678769877
   2.735231253200037  -0.114980181265741
  -0.022597643298814   2.569972576404279];


E =1.0e+003 *[-0.1046036   0.0021717   0.0010000           0
   0.0003400  -0.1013957           0   0.0010000
  -2.7352062   0.1134581  -0.0000006  -0.0000000
   0.0172663  -2.5700319  -0.00000002 -0.0000001];


%x = [u; motor pos; ball pos; theta; r; thetaD; rD]
u    = x(1);
mpos = x(2);
rpos = x(3);
x1   = x(4);
x2   = x(5);
x3   = x(6);
x4   = x(7);

%Summing Junction of Observer
V1=E*[x1;x2;x3;x4];
V2=u*G;
V3=L*[mpos;rpos];
Integrate=V1+V2+V3;

%Observer Integration
Integral = [x1;x2;x3;x4] + dT*Integrate;

%VEL= [motor vel; ball vel; theta; r; thetaD; rD]
VEL = [Integral(3);Integral(4);Integral];
```

Appendix C - LabVIEW Controller

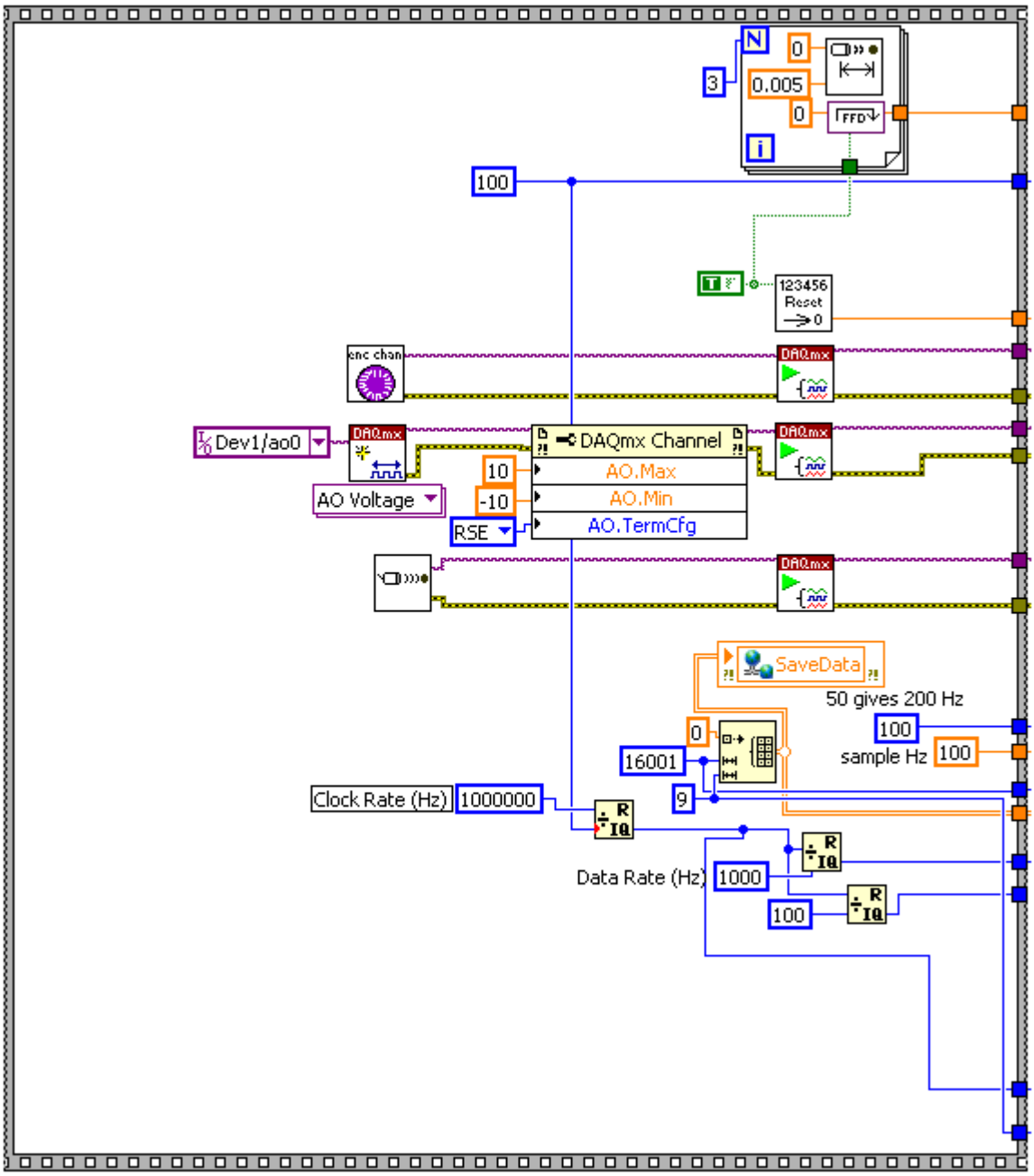

Figure C-1 Controller Initialization

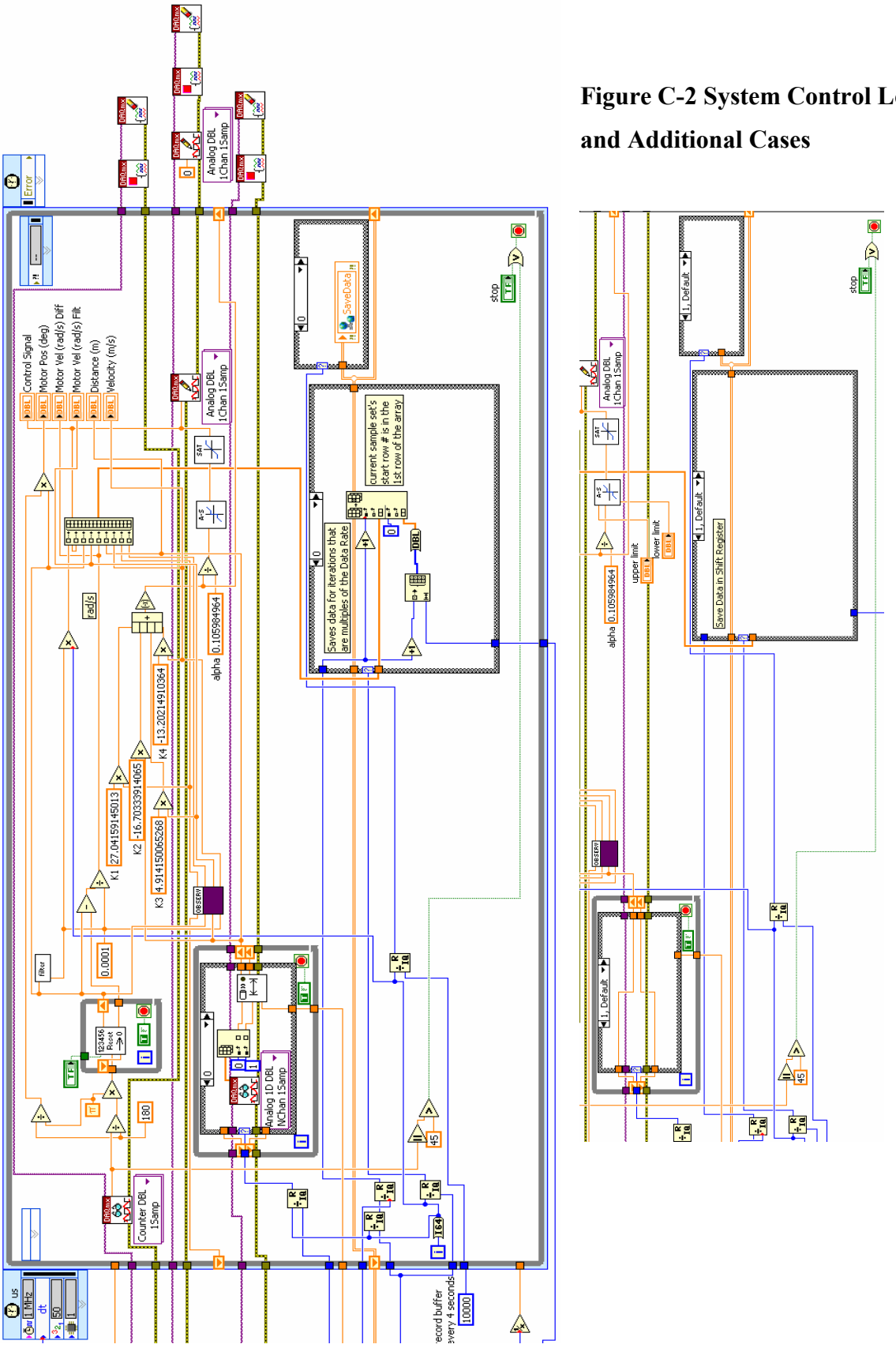

Figure C-2 System Control Loop and Additional Cases